

Climate Response to Aerosol Geoengineering: A Multimethod Comparison

HELENE MURI

*Section for Meteorology and Oceanography, Department of Geosciences, University of Oslo, Oslo, and
Industrial Ecology Program, Department of Energy and Process Engineering, Norwegian
University of Science and Technology, Trondheim, Norway*

JERRY TJIPUTRA, ODD HELGE OTTERÅ, MURALIDHAR ADAKUDLU, AND SIV K. LAUVSET

Uni Research Climate, Bjerknes Centre for Climate Research, Bergen, Norway

ALF GRINI AND MICHAEL SCHULZ

Meteorological Institute, Oslo, Norway

ULRIKE NIEMEIER

Max Planck Institute for Meteorology, Hamburg, Germany


JÓN EGILL KRISTJÁNSSON^a


Section for Meteorology and Oceanography, Department of Geosciences, University of Oslo, Oslo, Norway

(Manuscript received 20 September 2017, in final form 19 April 2018)

ABSTRACT

Considering the ambitious climate targets of the Paris Agreement to limit global warming to 2°C, with aspirations of even 1.5°C, questions arise on how to achieve this. Climate geoengineering has been proposed as a potential tool to minimize global harm from anthropogenic climate change. Here, an Earth system model is used to evaluate the climate response when transferring from a high CO₂ forcing scenario, RCP8.5, to a middle-of-the-road forcing scenario, like RCP4.5, using aerosol geoengineering. Three different techniques are considered: stratospheric aerosol injections (SAI), marine sky brightening (MSB), and cirrus cloud thinning (CCT). The climate states appearing in the climate geoengineering cases are found to be closer to RCP4.5 than RCP8.5 and many anthropogenic global warming symptoms are alleviated. All three techniques result in comparable global mean temperature evolutions. However, there are some notable differences in other climate variables due to the nature of the forcings applied. CCT acts mainly on the longwave part of the radiation budget, as opposed to MSB and SAI acting in the shortwave. This yields a difference in the response, particularly in the hydrological cycle. The responses in sea ice, sea level, ocean heat, and circulation, as well as the carbon cycle, are furthermore compared. Sudden termination of the aerosol injection geoengineering shows that the climate very rapidly (within two decades) reverts to the path of RCP8.5, questioning the sustainable nature of such climate geoengineering, and simultaneous mitigation during any such form of climate geoengineering would be needed to limit termination risks.

 Denotes content that is immediately available upon publication as open access.

 Supplemental information related to this paper is available at the Journals Online website: <https://doi.org/10.1175/JCLI-D-17-0620.s1>.

^a Deceased.

Corresponding author: Helene Muri, helene.muri@ntnu.no

DOI: 10.1175/JCLI-D-17-0620.1

© 2018 American Meteorological Society. For information regarding reuse of this content and general copyright information, consult the [AMS Copyright Policy](#) (www.ametsoc.org/PUBSReuseLicenses).

1. Introduction

The Paris Agreement was adopted by consensus at the United Nations Framework Convention on Climate Change (UNFCCC) Conference of the Parties in Paris in 2015. At the heart of this agreement is the objective of limiting global temperature increase to 2°C compared to the preindustrial era, with the ambition to pursue efforts to limit the temperature increase even further to 1.5°C (UNFCCC 2015). Such ambitious goals need strong mitigation efforts, and must likely be accompanied by large-scale carbon capture and storage technologies toward the end of the century (Clarke et al. 2014). As potential complementary tools, climate geoengineering techniques have been proposed to minimize global harm from anthropogenic climate change with potential to contribute toward reaching the Paris Agreement goals (Lawrence et al. 2018, manuscript submitted to *Nat. Commun.*). Among such complementary efforts to mitigation exists a set of approaches that do not directly address the root of the problem, greenhouse gases and CO₂ in particular. In contrast, they act to reduce surface temperatures by affecting the global radiation budget via, for instance, atmospheric aerosol additions and are often referred to as solar radiation management (Shepherd et al. 2009) or albedo modification (National Research Council 2015). Here we use the term *aerosol geoengineering*, as the approaches considered are all based on the concept of modifying Earth's radiation budget by the addition of aerosols to the atmosphere. The methods are directed at both the shortwave and the longwave parts of the radiation budget. We use an Earth system model to evaluate the radiative potential to transfer from a high CO₂ forcing scenario, representative concentration pathway 8.5 (RCP8.5), to a medium scenario, RCP4.5, via stratospheric aerosol injections (SAI), marine sky brightening (MSB), and cirrus cloud thinning (CCT) individually.

The perhaps most studied aerosol geoengineering approach is based on the addition of aerosols to form a reflective layer in the stratosphere, as proposed by Kellogg and Schneider (1974) and Budyko (1977), with accelerated research after Crutzen (2006). The idea is to spray aerosols, or gaseous precursors like SO₂, into the lower stratosphere to form a layer of reflective particles, which is an analog to the dimming aerosol blankets observed after explosive volcanic eruptions (e.g., Robock et al. 2013). The aerosols would increase the amount of reflected solar radiation and hence cool the climate. It has been suggested that sulfuric acid and sulfur may be combined to achieve an optimal size distribution of aerosols (Benduhn et al. 2016), and other compositions are also being considered (e.g.,

Weisenstein et al. 2015). Stratospheric aerosol injection has been deemed the most promising method in terms of cooling potential (Boucher et al. 2013) and assumed technological feasibility (McClellan et al. 2012).

Another proposed approach aims at increasing the reflectivity of clouds over the oceans, often called marine cloud brightening (Latham 1990). The method draws upon the natural capacity of sea salt to act as cloud condensation nuclei (CCN). Increasing the emissions of sea salt from the oceans would provide more CCN and increase the number of droplets in a cloud. Higher concentration of smaller cloud droplets increases the surface area of the clouds and hence increases its reflectivity, often referred to as the first indirect aerosol effect, the Twomey effect after Twomey (1977), or the cloud albedo effect. It has been suggested that the flux of salt from the oceans could be increased by pumping up and spraying filtered seawater (Salter et al. 2008). As the water evaporates and sea salt aerosols are generated, the direct effect of the sea salt will also play a role (Ahlm et al. 2017). Considering both the first direct and indirect effects of the sea salt aerosols, one may also call this approach marine “sky” brightening (Schäfer et al. 2015; Muri et al. 2015).

The third aerosol geoengineering approach considered in this study is cirrus cloud thinning, which was first proposed by Mitchell and Finnegan (2009). As opposed to the above-mentioned methods, cirrus cloud thinning primarily acts on the longwave radiation. High, thin ice clouds have a net warming effect on the climate, as they trap longwave radiation (Lee et al. 2009). The idea is therefore to reduce the emissivity and lifetimes of these clouds in order to let more longwave radiation escape the atmosphere. This could, in theory, be achieved by seeding the clouds and cloud forming regions with highly effective ice nuclei to draw upon the competition effect between homogeneous and heterogeneous freezing. Heterogeneous freezing can occur at lower supersaturations than homogenous freezing. Hence introducing potent ice nuclei in regions dominated by homogeneous freezing, or with low ambient concentrations of suitable ice nuclei like mineral dust, one could initiate freezing and grow larger and fewer ice crystals than otherwise. As the ice crystals grow larger, the terminal velocity increases and they would eventually sediment out of the upper troposphere. The location and purity of the cirrus clouds would determine where this method would be the most effective. This depletes not only cirrus clouds, but also upper tropospheric water vapor (Muri et al. 2014), which is a powerful greenhouse gas.

Here, we assess the climate response to the three approaches described above using an Earth system model.

This is the first comprehensive, in-depth multimethod Earth system model study of the comparative climate consequences of aerosol-based climate geoengineering with all model components being analyzed in a comprehensive manner, including atmosphere, sea ice, ocean circulation, and the carbon cycle. So far, there have only been a few publications comparing the climate responses to different methods of aerosol climate geoengineering. Considering the limited number and scope of these studies, there is clearly a need for more in-depth comparative analysis of these types of climate geoengineering in a consistent framework. Crook et al. (2015) focused on the annual mean temperature and precipitation responses to several methods, including the three considered here. They found that all three approaches lead to regional precipitation rate changes, in particular in the tropics, induced by changes in the atmospheric circulation resulting from the forcings applied. Niemeier et al. (2013) focused on the precipitation response to shortwave-based methods and found that MSB leads to the strongest reduction in the global mean, as the forcing is applied over the oceans. This suppresses the evaporation rates and hence the precipitation. Aswathy et al. (2015) investigated changes to climate extremes from SAI and MSB. Both methods gave a reduction in cold extremes at high latitudes, as these methods are not effective during the polar nights. SAI was found to be more effective than MSB at inhibiting extreme precipitation events over land, since the MSB forcing tends to increase precipitation over extratropical land. Jones et al. (2011) found that marine cloud brightening leads to a more spatially heterogeneous climate response than SAI due to the more regional application of the forcing from cloud brightening. Considering the limited number and scope of these studies, there is clearly a need for more in-depth comparative analysis of these types of climate geoengineering.

This article is outlined as follows: the Earth system model and the experiment design are described in section 2. Results, including atmosphere, variability modes, ocean, carbon cycle, and biogeochemistry responses are presented in section 3, and conclusions are drawn in section 4.

2. Model and experiment design

The fully coupled Norwegian Earth System Model, NorESM1-ME, is used here (Tjiputra et al. 2013, 2016). The same model contributed to phase 5 of the Coupled Model Intercomparison Project (CMIP5) and to several articles that were referred to in the Intergovernmental Panel on Climate Change (IPCC) Fifth Assessment Report. It is run at a horizontal resolution of 1.9°

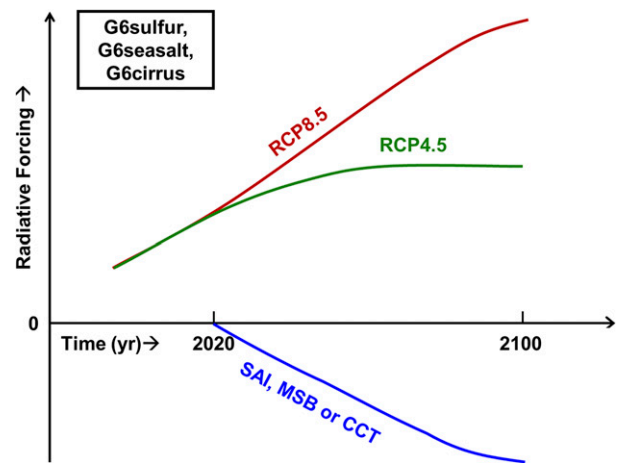


FIG. 1. Schematic of the experiments. Three aerosol geoengineering approaches were applied individually to offset the anthropogenic radiative forcing from RCP8.5 down to RCP4.5 levels. The approaches considered are stratospheric aerosol injections (SAI), marine sky brightening (MSB), and cirrus cloud thinning (CCT).

latitude \times 2.5° longitude, with 26 vertical levels in the atmosphere, while the ocean model has $1^\circ \times 1^\circ$ horizontal resolution and 53 isopycnic layers.

The experiments were designed such that the anthropogenic radiative forcing of the RCP8.5 scenario is reduced to that of RCP4.5 (Fig. 1) through the increasing application of aerosol geoengineering. The Geoengineering Model Intercomparison Project (GeoMIP) has adopted a similar design for their “G6sulfur” experiment, as outlined in Kravitz et al. (2015). The experiment was designed at a time when anthropogenic emissions were overshooting RCP8.5, a while before the Paris Agreement was signed. It represents a future where mitigation efforts fail and alternative measures to ameliorate global warming would be required. RCP8.5 and RCP4.5 have been the subject of extensive analysis (e.g., Tebaldi and Wehner 2018; Oleson et al. 2018; O’Neill et al. 2018) and will hence not form the primary focus of the analysis here. The aerosol geoengineering is applied here in year 2020 on the background of the RCP8.5 scenario and continued for 81 years. Three realizations of each experiment were carried out by perturbing the initial conditions at the start of each simulation. The climate response is determined for the model years 2060–89 in parts of our analysis. In the year 2101 (i.e., when the RCPs are no longer well defined in terms of aerosol emissions and land use change) the aerosol geoengineering was terminated in the model. One realization of each experiment was continued for another 50 years. With the exception of land use change, which is kept constant at year 2100 conditions, the extensions follow the extended concentration pathway 8.5 (Meinshausen et al. 2011). This allows us to address the so-called termination effect. A Student’s t test

TABLE 1. The experiments performed with NorESM1-ME.

Experiment name	Realizations	Details
Historical	1	CMIP5 historical simulation.
RCP4.5	3	RCP4.5 scenario, as per CMIP5 (Meinshausen et al. 2011).
RCP8.5	3	RCP8.5 scenario, as per CMIP5 (Meinshausen et al. 2011).
RCP8.5 + SAI	3	Stratospheric aerosols on the background of RCP8.5, with prescribed sulfate aerosol concentrations in the years 2020–2100.
RCP8.5 + SAItxt	1	50-yr continuation to SAI starting in 2101, with the climate engineering switched off.
RCP8.5 + MSB	3	Marine cloud brightening by increasing accumulation mode sea salt emissions over $\pm 45^\circ$ in the years 2020–2100.
RCP8.5 + MSBtxt	1	50-yr continuation to MSB starting in 2101, with the climate engineering switched off.
RCP8.5 + CCT	3	Cirrus cloud thinning by increasing the ice crystal fall speeds in the years 2020–2100.
RCP8.5 + CCTxt	1	50-yr continuation to CCT starting in 2101, with the climate engineering switched off.

was done to assess the statistical significance of the results using a p value of 0.05, assuming equal variance, on the ensemble mean temporal data. An overview of the experiments is found in Table 1.

Aerosol geoengineering experiments

1) STRATOSPHERIC AEROSOL INJECTIONS (RCP8.5 + SAI)

NorESM1-ME does not include an interactive stratospheric aerosol module. Therefore, we used aerosol properties in the same way as described in Tilmes et al. (2015). SO_2 was injected at around 20-km height (60 hPa) in a grid point close to the equator. The evolution of sulfate aerosol was calculated using an interactive aerosol microphysics module (HAM) within the general circulation model ECHAM5 (Niemeier et al. 2011). The distribution of the aerosols and resulting aerosol optical depth are described in Niemeier and Timmreck (2015). The ECHAM5-HAM dataset provides stratospheric zonal aerosol extinction, single-scattering albedo, and asymmetry factors. Different sensitivity tests were done in order to find the amounts of aerosols needed in NorESM1-ME to offset the anthropogenic forcing of RCP8.5 to RCP4.5. The aerosol emission strengths needed was found to be of 5 Tg(S) yr^{-1} in 2050, scaling up to 10 Tg(S) yr^{-1} in 2075 and 20 Tg(S) yr^{-1} in 2100.

2) MARINE SKY BRIGHTENING (RCP8.5 + MSB)

NorESM1-ME has a fully prognostic treatment of sea salt aerosol emissions and their coupling to cloud droplet number concentrations (CDNC). Marine sky brightening was here done by increasing the natural emissions of sea salt aerosols at the ocean surface uniformly over latitudes between $\pm 45^\circ$. Our method follows Alterskjær et al. (2013), only here we increase emissions over a larger ocean area to enable reaching a radiative forcing of -4 W m^{-2} more easily. Emissions were increased for the aerosols in the accumulation mode with a dry number modal radius of $0.13 \mu\text{m}$ and a geometric standard deviation of 1.59, which

corresponds to a dry effective radius of $0.22 \mu\text{m}$, as this mode has been found to be the most effective at increasing the shortwave cloud forcing in the model (Alterskjær and Kristjánsson 2013). Total emission increases needed over $\pm 45^\circ$ latitude in the year 2100 were on the order of $\sim 460 \text{ Tg yr}^{-1}$ of sea salt.

3) CIRRUS CLOUD THINNING (RCP8.5 + CCT)

For the representation of cirrus cloud thinning in the model, the method of Muri et al. (2014) was adopted. The terminal velocity of all ice crystals for temperatures colder than -38°C , which is the typical temperature at which homogeneous freezing can occur, was increased. Because of the simplified parameterization of cirrus cloud formation in the model, this idealized representation of ice cloud thinning is used. Although some important microphysical processes are missing in the representation of cirrus cloud thinning, earlier studies have found that the fundamental surface climate response is representative compared to simulations with a more complex parameterization of ice cloud processes (Muri et al. 2014; Storelvmo et al. 2013). The ice cloud coverage in NorESM has been evaluated by Li et al. (2012), who found it to be reasonable compared to satellite observations and indeed one of the better-performing CMIP5 models in this regard. At 600 mb, observations show ice water content (IWC) of 4.5 mg kg^{-1} and NorESM 5.5 mg kg^{-1} over the northern and southern high latitudes, 5.5 and 8 mg kg^{-1} , respectively. The ice crystal fall speed was scaled up by a factor of 10 by the end of the century, keeping it within the observed range of fall speeds (Mitchell 1996; Gasparini et al. 2017).

3. Results

a. Atmospheric response

The resulting radiative flux imbalance at the top of the atmosphere (TOA; Fig. 2a) shows that the aerosol injection geoengineering experiments are close to that of RCP4.5 (within $\pm 0.1 \text{ W m}^{-2}$ in the decadal means),

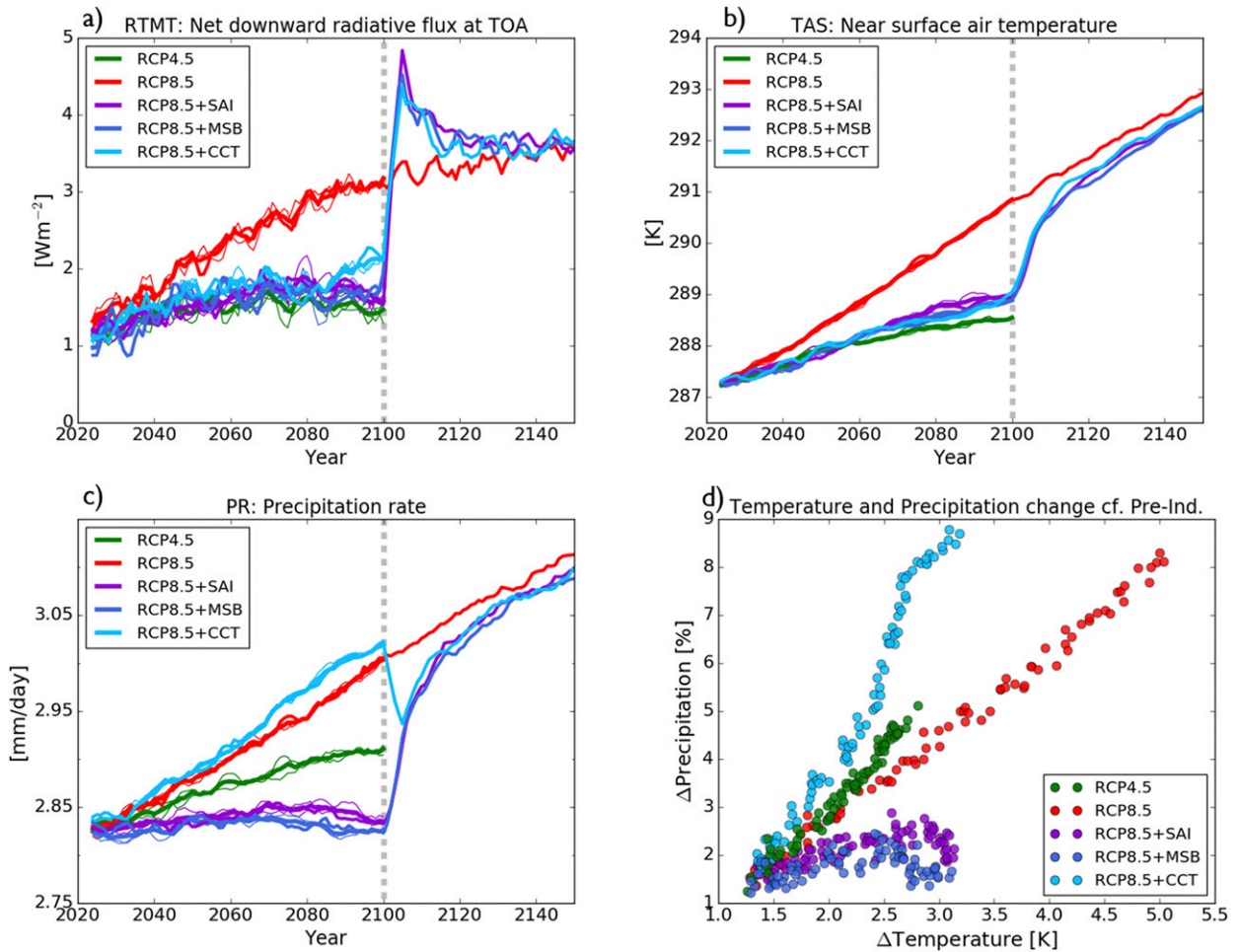


FIG. 2. Time series of 5-yr running mean global annual mean (a) radiative flux imbalance at the top of the atmosphere ($W m^{-2}$), (b) near-surface air temperature (K), and (c) precipitation rate ($mm day^{-1}$). (d) Temperature change (K) vs precipitation change (%) compared to the preindustrial; each dot is one model year. Red curves: RCP8.5, green: RCP4.5, purple: RCP8.5 + SAI, dark blue: RCP8.5 + MCB, and light blue: RCP8.5 + CCT. Thin lines represent each ensemble member, while thicker lines are the ensemble means. Vertical dashed gray lines indicate time of termination of climate geoengineering.

except during the last decade in the case of RCP8.5 + CCT. The maximum achievable effective radiative forcing for this method in this model was estimated to be about $-3.8 W m^{-2}$, because the amount of susceptible cirrus clouds, and fall speed of ice crystals cannot reasonably be expanded further. Hence, the RCP8.5 + CCT ensemble members have a somewhat higher radiation imbalance at TOA toward the end of the twenty-first century than the other methods, which are able to achieve the required $-4.0 W m^{-2}$ in year 2100.

The global 5-yr running mean near-surface air temperatures (Fig. 2b) reveal that in all the climate geoengineering experiments, the temperatures are close to that of RCP4.5, although they show some additional warming. This additional heat, in particular in the beginning of the geoengineering period, is partly due to the fact that they branch off from RCP8.5 in year 2020 and

hence accumulate a higher total heat content than RCP4.5, in particular through accumulation of heat in the ocean in the period 2005–20 when the RCP pathways are already different. Given the thermal inertia of the climate system, this becomes also evident during the mid to late century. However, Table 2 shows also that the net TOA radiation flux is on average slightly more positive, which may reflect that the overall effective radiative forcing was positive in the aerosol geoengineering experiments, as compared to the RCP4.5 experiment, which will be further discussed in section 3d. Upon termination of the aerosol geoengineering in year 2100, there is a very rapid response to this instantaneous $+4.0 W m^{-2}$ forcing (Figs. 2a–c). This is from rapid adjustments in water vapor and clouds, increasing the downward radiative flux (e.g., Kravitz et al. 2013; Andrews et al. 2009; Andrews and Forster 2010). There is also

TABLE 2. Global annual mean changes relative to RCP4.5 in key variables for the years 2060–89. Tas: near-surface air temperature, Pr: precipitation rate, RTMT: Net downward flux at TOA, CLDTOT: total cloud fraction.

Variable	RCP8.5	RCP8.5 + SAI	RCP8.5 + MSB	RCP8.5 + CCT
Tas (K)	1.34	0.32	0.21	0.16
Pr (mm day ⁻¹)	0.049	-0.044	-0.059	0.071
RTMT (W m ⁻²)	1.19	0.21	0.08	0.27
CLDTOT (fraction)	0.0017	-0.0057	-0.0072	-0.0455

reduction in atmospheric stability, when the SW-absorbing stratospheric aerosol layer is removed, increasing the latent heat fluxes, giving an increase in net TOA radiative fluxes (Fig. 2a).

RCP8.5 is warmer everywhere compared to RCP4.5 over the period of 2060–89 with a polar amplification of the warming (Fig. 3a). There is heat remaining in the Arctic in the annual mean in the aerosol geoengineering cases compared to RCP4.5 (Figs. 3b–d). This is particularly evident in the shortwave (SW)-based methods with a warming of 1–2 K in places (Figs. 3b,c), considering the lower amount of incoming solar radiation and the methods are not effective during the polar nighttime in particular. As noted in Schmidt et al. (2012), the latitudinal distribution of greenhouse gas forcing and that of SW-based climate geoengineering forcing are different. When combined in, for example, a SAI-RCP4.5 scenario, this results in more positive forcing in polar regions, balanced by negative forcing in tropical and midlatitude bands, as reflected in Fig. 4b. Amplifications from positive feedbacks such as reduced sea ice (section 3c) and snow cover (see Fig. S1 in the online supplemental material) enhance this uneven forcing distribution. Varying the aerosol injection strength seasonally and latitudinally as per, for example, Kravitz et al. (2017), would possibly avoid some of the Arctic “residual warming” issue associated with the SW reflecting methods. Even more constrained in regional extent is the RCP8.5 + MSB forcing, being exerted between $\pm 45^\circ$ latitude. There is a cooling compared to RCP4.5 over some parts of the oceans in the RCP8.5 + MSB case (Fig. 3c), since this is where the climate geoengineering forcing is the strongest, indicated by the negative net fluxes at TOA (Fig. 4c). The cooling is of -0.2 to -0.5 K in the tropical and northwest Pacific and mostly insignificant in the Atlantic. The global mean warming in years 2060–89 compared to RCP4.5 is of 0.21 K in the RCP8.5 + MSB case and 0.32 K in the RCP8.5 + SAI case. In the RCP8.5 + CCT experiment (Fig. 3d), the global mean temperatures are closer to RCP4.5 and only 0.16 K warmer (Table 2). A hemispheric asymmetry appears, with cooling relative to RCP4.5 in the Southern Hemisphere (SH) and higher temperatures in the Northern Hemisphere (NH). We associate this with a

higher volume of very cold air masses over the SH, particularly toward the pole, with a high cover of cirrus clouds in NorESM1-ME. This leads to a strong negative poleward SH regional forcing, as reflected in Fig. 4d, with near-surface air temperatures cooling by -2 to -3 K compared to RCP4.5. The cirrus coverage is not as high in the NH, where the unabated greenhouse gas (GHG) warming trumps the RCP8.5 + CCT cooling. The cooling asymmetry is a caveat of the experiment design, where we are targeting the global mean radiative forcing.

The global annual mean temperature versus precipitation changes relative to the preindustrial simulation (Fig. 2d) shows that for a 2-K global warming (cf. the targets of the Paris Agreement) there is a $\sim 3\%$ increase in precipitation for the global warming cases of RCP4.5 and RCP8.5. The precipitation increases more per degree warming in RCP4.5; compare RCP8.5 in the later decades of the century, when there is a reduction in the emissions of short-lived climate pollutants (SLCP) in RCP4.5. These SLCP act to inhibit precipitation through the second indirect aerosol effect (Albrecht 1989). Hence, cleaning up these emissions increases the precipitation rates. For the SW-based methods the precipitation increases are limited to $\sim 2.4\%$ or less, while for the RCP8.5 + CCT the increase is even greater than the 3% increase. The precipitation rates are suppressed in the SW-based methods compared to RCP4.5 in the global 5-yr running mean (Fig. 3c and Fig. S2), as the reduction in incoming solar radiation at the surface reduces the latent heat release. This has also been found in previous studies (e.g., Aswathy et al. 2015; Alterskjær et al. 2013; Niemeier et al. 2013). This suppression is stronger in the RCP8.5 + MSB case, as the forcing is applied over the oceans and that is where the strongest evaporation rates occur, and is responsible for the amplitude of the global hydrological cycle. As for RCP8.5 + CCT, the precipitation rates are increased, even compared to RCP8.5. As described in Kristjánsson et al. (2015), when the atmosphere is losing longwave (LW) radiation, there is an increase in the latent heat flux as the atmosphere is trying to restore its radiative convective equilibrium, amplifying the hydrological cycle.

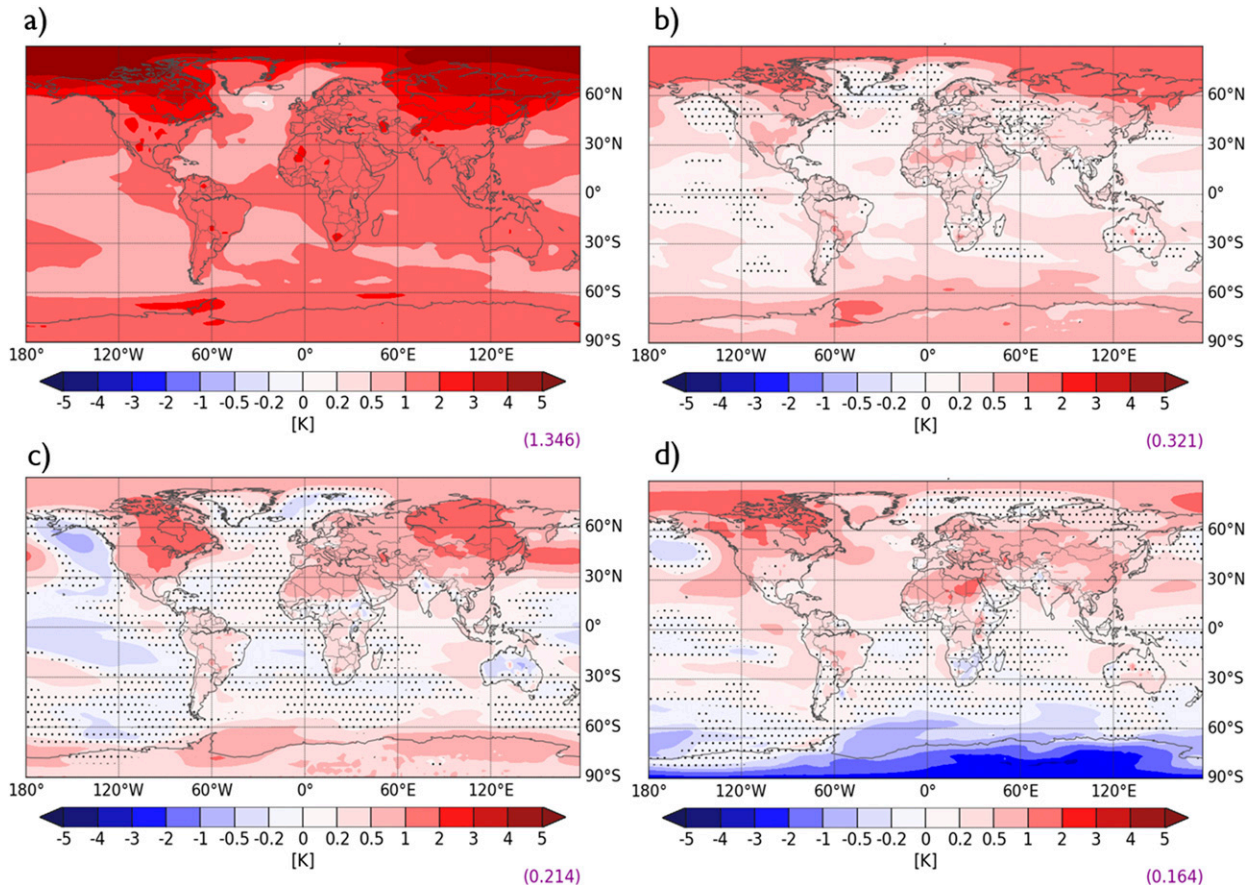


FIG. 3. Annual mean near-surface air temperature difference from RCP4.5 (K): (a) RCP8.5, (b) RCP8.5 + SAI, (c) RCP8.5 + MSB, and (d) RCP8.5 + CCT. Means over all three ensemble members for each experiment over years 2060–89. Nonstippling indicates a confidence level higher than 95% following the Student’s t test. Global mean values in purple.

The spatial pattern of hydrological cycle changes show a familiar global warming effect in the RCP8.5 case (Fig. 5a), with drier conditions in the subtropical high pressure regions from a widening of the Hadley cell and poleward stretching of these subtropical dry zones, wetter conditions elsewhere (Collins et al. 2013). For RCP8.5 + SAI, there is less change regionally when reductions in evaporative demands are taken into account (Fig. S3b) as compared to when considering precipitation changes only (Fig. S2b). The cooling relative to RCP4.5 of the SH and slight warming of the NH in the RCP8.5 + CCT case gives an increase in the thermal gradient between the hemispheres and hence a northward displacement of the intertropical convergence zone (Fig. 5d). Differential heating of the hemispheres is a known driver of the location of the rain belt (e.g., Broccoli et al. 2006; Chiang and Bitz 2005; Vellinga and Wood 2002). As for marine sky brightening (Fig. 5c), there is a change in circulation, increasing the hydrological cycle intensity over land in the tropics and parts of the extratropics accompanied with a weakening over

nearby oceans. As the forcing is applied over the oceans, there is an increase in the land–sea thermal gradient (Fig. 3c), inducing a “monsoon-like” response, which has also been found by Bala et al. (2009), Niemeier et al. (2013), and Alterskjær et al. (2013) and in the GeoMIP ensemble (Ahlm et al. 2017; Stjern et al. 2018). These changes are also confirmed by the changes in total cloud cover fraction (Fig. S4c) and in the TOA radiative flux imbalance (Fig. 4c).

b. North Atlantic Oscillation

To understand the influence of aerosol geoengineering on the regional aspects of atmospheric circulation, we focus on the characteristics and patterns associated with the North Atlantic Oscillation (NAO). The NAO, which is a fluctuation in the surface pressure at the Azores high and Icelandic low, happens to be the dominant variability mode in the North Atlantic that influences the regional climate significantly (e.g., Hurrell et al. 2003). The NAO is defined as the leading empirical orthogonal function (EOF) mode of the

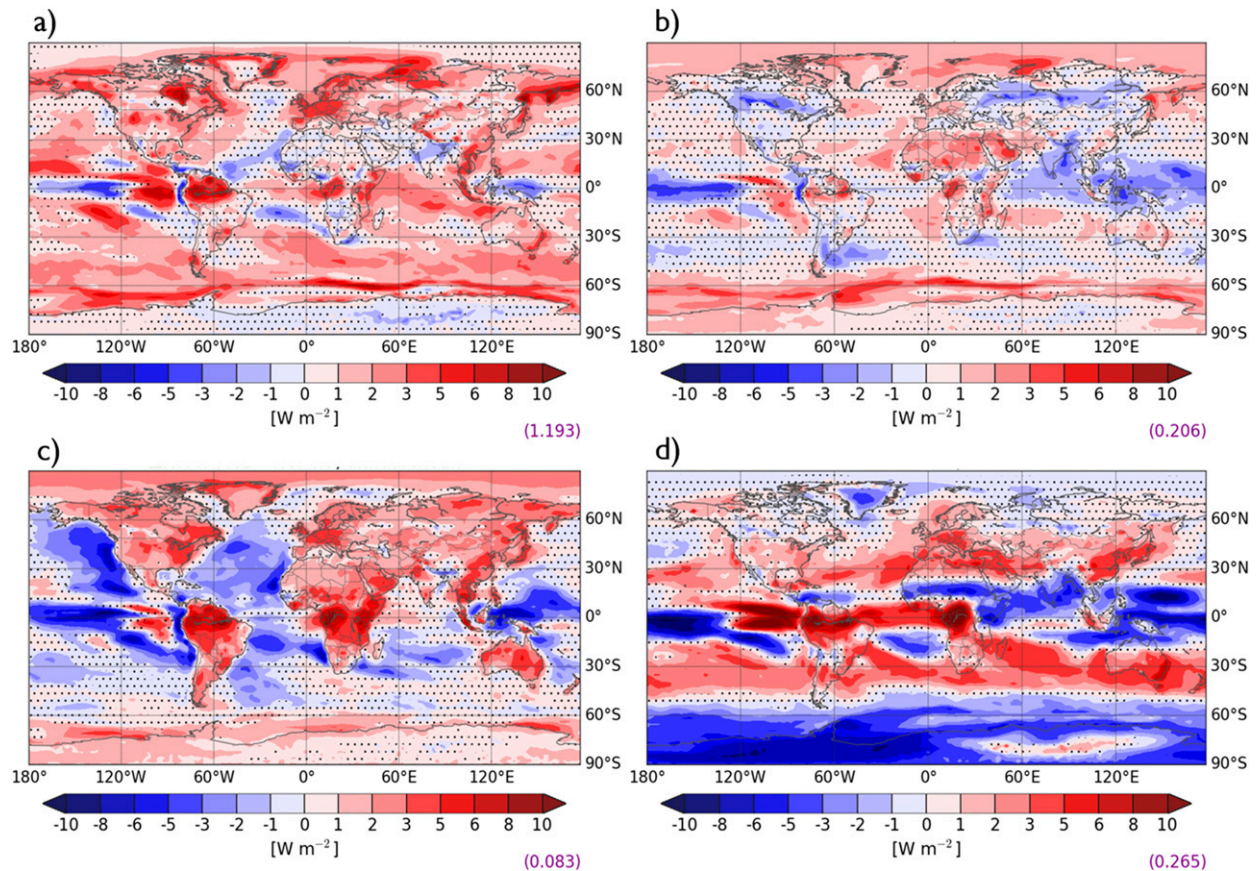


FIG. 4. Annual mean radiative flux imbalance at the TOA difference from RCP4.5 (W m^{-2}); (a) RCP8.5, (b) RCP8.5 + SAI, (c) RCP8.5 + MSB, and (d) RCP8.5 + CCT. Means over all three ensemble members for each experiment over years 2060–89. Nonstippling indicates a confidence level higher than 95% following the Student's t test. Global mean values in purple.

monthly winter [December–March (DJFM)] mean sea level pressure (MSLP) anomalies for the North Atlantic (20° – 90° N, 90° W– 40° E).

Figure 6 shows the spatial patterns of the leading NAO EOF mode for years 2060–89. The warming signal in the RCP8.5 scenario compared to RCP4.5 is associated with intensification in the NAO signal and a tendency for a breakdown of the southern high amplitude mode. The intensification of NAO under RCP8.5 has also been identified by Hanna et al. (2014). This feature is further strengthened compared to both RCP4.5 and RCP8.5 in the stratospheric aerosol injection experiment, where the NAO signal is the strongest in spite of the tropospheric cooling identified in this experiment in section 3a. This can be attributed to the increase in the localized equatorial heating in the lower stratosphere, as shown in Fig. S5, resulting from the absorption of near-infrared and longwave radiation due to the presence of stratospheric aerosols. The anomalous temperatures thus formed strengthen the meridional gradient in the lower stratosphere, which leads to stronger zonal winds

and a deeper stratospheric polar vortex, followed by strong NAO circulation in the troposphere. This outcome is consistent with some of the earlier studies, where strengthening of the NAO is identified following volcanic eruptions (e.g., Stenchikov et al. 2002; Driscoll et al. 2012). The RCP8.5 + MSB and RCP8.5 + CCT cases do not show considerable changes in the NAO intensity with respect to the RCP8.5 case, and are intensified compared to RCP4.5, with the spatial pattern of the NAO signal being similar to the RCP4.5 scenario. The variance of the NAO index is discussed in the online supplemental material and shown in Fig. S6.

The changes in the NAO are accompanied by changes in the surface climate, in terms of 2-m air temperature and precipitation, high minus low NAO composites, as shown in Figs. 7 and 8 respectively. The RCP4.5 case displays a typical positive phase of the NAO, where intensified pressure gradient between the lower and higher latitudes enhances the surface westerlies across the Atlantic into Europe. This brings warm and wet conditions over Scandinavia and northern Europe, while

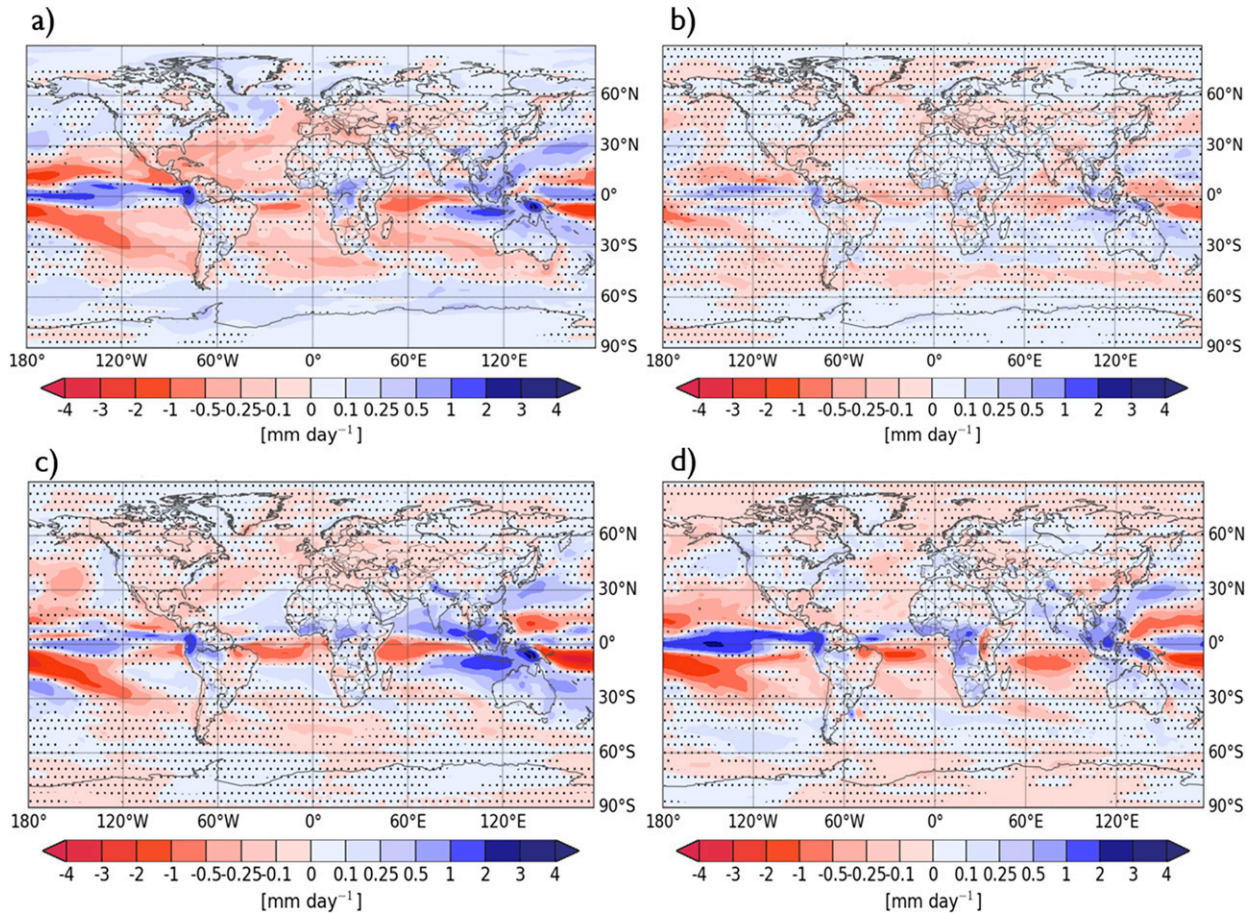


FIG. 5. Annual mean precipitation minus evaporation rate difference (mm day^{-1}) from RCP4.5: (a) RCP8.5, (b) RCP8.5 + SAI, (c) RCP8.5 + MSB, and (d) RCP8.5 + CCT. Means over all three ensemble members for each experiment over years 2060–89. Non-stippling indicates a confidence level higher than 95% following the Student's t test.

southern Europe and Greenland experience cold and dry conditions due to the advection from the polar regions. With the Arctic being warmer in the RCP8.5 scenario, the temperatures over Baffin Bay and parts of northeast Canada rise by $\sim 3\text{K}$ in comparison to the RCP4.5 case, whereas the temperature over Scandinavia remains largely unchanged. The inclusion of stratospheric aerosols leads to cooler surface temperatures compared to RCP4.5 over Scandinavia. This is attributable to the structural modifications to NAO in the RCP8.5 + SAI case. The positioning of the southern center of action causes the advection of cooler temperatures from midlatitudes in the SAI case whereas the westerlies advect warmer temperatures from northeast United States and Canada in the rest of the cases (the regional temperature differences are evident in Fig. 3). The RCP8.5 + MSB forcing drives the temperature patterns closer to the RCP4.5 case, whereas the RCP8.5 + CCT response appears closer to RCP4.5 except for North Atlantic and central Europe.

The precipitation changes have a tripole pattern in RCP4.5, with dry regions over southern Europe and the western Atlantic, and wet regions over North Atlantic including coastal Norway (Fig. 8). No significant change can be seen in RCP8.5 compared to RCP4.5. In the case of aerosol geoengineering, RCP8.5 + CCT and RCP8.5 + MSB see a stronger drying over Iberia, with little change over the European sector compared to RCP4.5. RCP8.5 + SAI has some notable differences compared to RCP4.5, including drier regions over the northeastern United States and southern Europe, consistent with the corresponding NAO pattern.

c. Sea ice and ocean responses

The NorESM1-ME historical simulation captures fairly well the main characteristics of the observed seasonal cycle of sea ice area (Fig. 9), as well as the observed sea ice extent for both March and September (Fig. 10). The sea ice extent is generally somewhat overestimated for the SH, in particular during austral

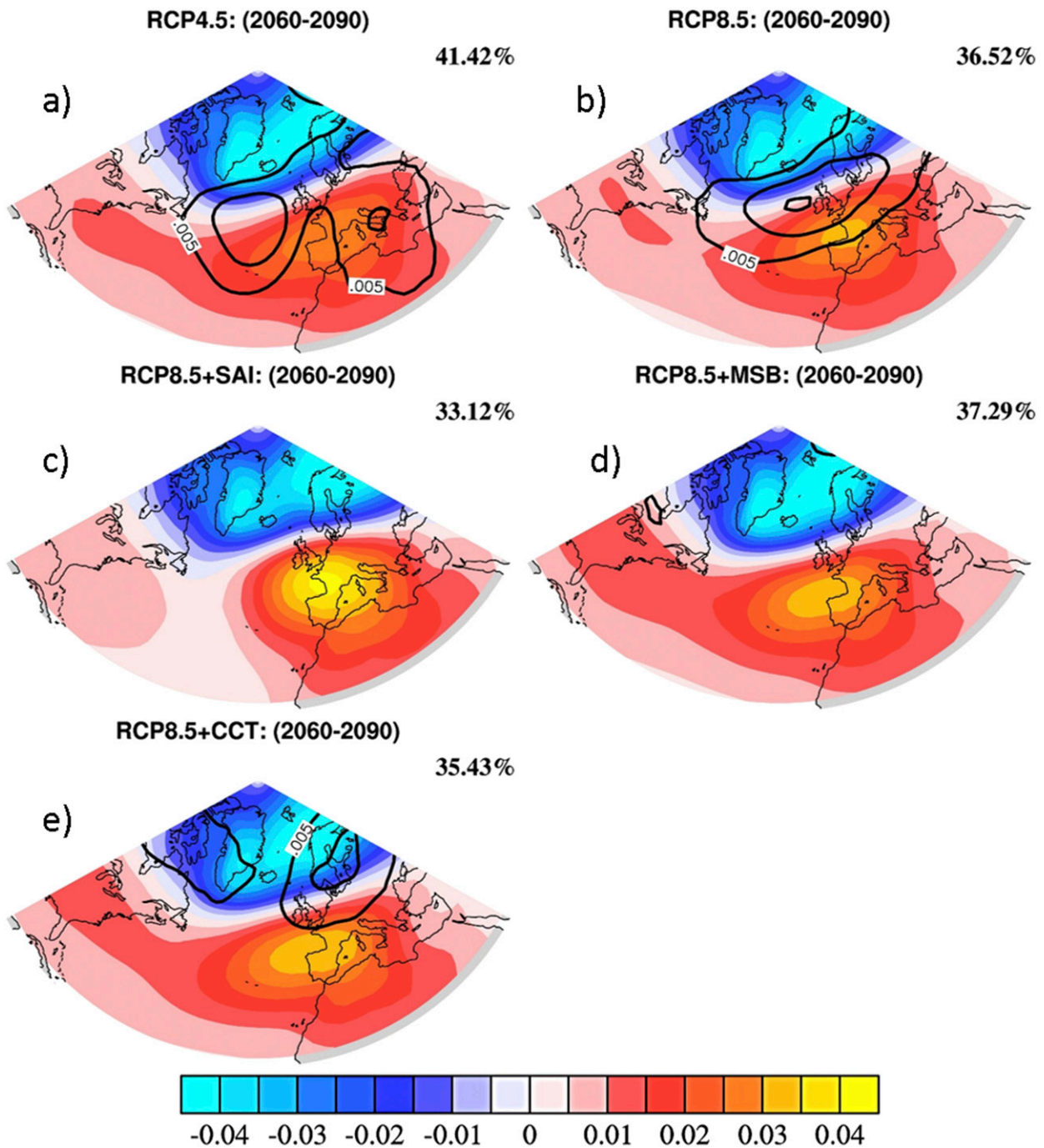


FIG. 6. Ensemble mean of the leading EOF (normalized) of monthly winter (DJFM) mean sea level pressure anomalies (Pa) for different scenarios. Black contours indicate the ensemble standard deviation (starting with 0.005 at an interval of 0.005). Numbers on top right indicate the variance explained by the corresponding EOF pattern.

summer and fall, with a bias of about 15% compared to the observed annual mean value. For the NH, the sea ice is slightly underestimated, in particular during boreal winter and spring, with a bias of about 9% compared to the observed annual value. In RCP8.5, the Arctic

becomes nearly ice-free during late summer and early autumn in the 2060–89 mean, with only a small region of sea ice remaining north of Greenland (Figs. 9a and 10b). In RCP4.5, the annual sea ice extent minimum is reduced to $3 \times 10^6 \text{ km}^2$ in September, a reduction of about

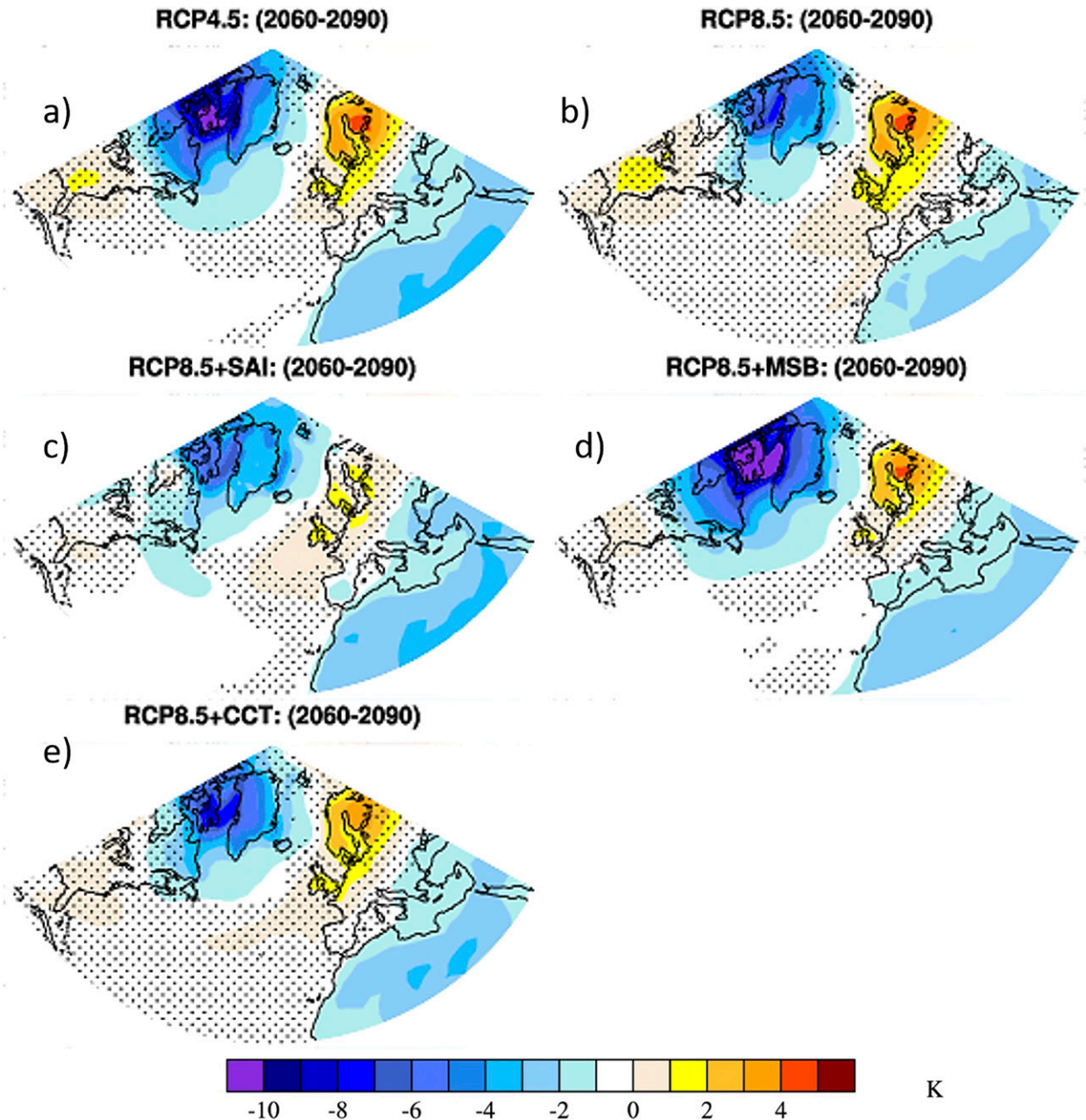


FIG. 7. DJFM near-surface temperatures (K) for high minus low NAO composites. Only the indices greater than ± 1 standard deviation are considered for estimating the difference. Significant differences, at 95% confidence level following the Student's *t* test, are hatched.

4×10^6 km² compared to observations from National Snow and Ice Data Center (NSIDC) over the period 1979–2005 (Cavalieri et al. 1996). All methods of aerosol geoengineering preserve the Arctic sea ice cover at the level of RCP4.5 throughout the winter and spring. There are still some losses, however, in the summer and autumn compared to RCP4.5, of about 0.5 – 0.75×10^6 km² in September (Fig. 9a). These reductions are likely related to the regional temperature changes and the polar

amplification, as discussed in section 3a. In the SH, the SW-based methods, RCP8.5 + SAI and RCP8.5 + MSB, lose more ice than RCP4.5 in the summer and autumn (Fig. 9b). By contrast, the RCP8.5 + CCT simulation increases the Antarctic sea ice extent compared to the baseline, RCP4.5, throughout the year. This is linked to the cooling compared to RCP4.5 discussed in section 3a.

Ocean heat content changes are very closely tied to the net radiative imbalance of the planet due to the large

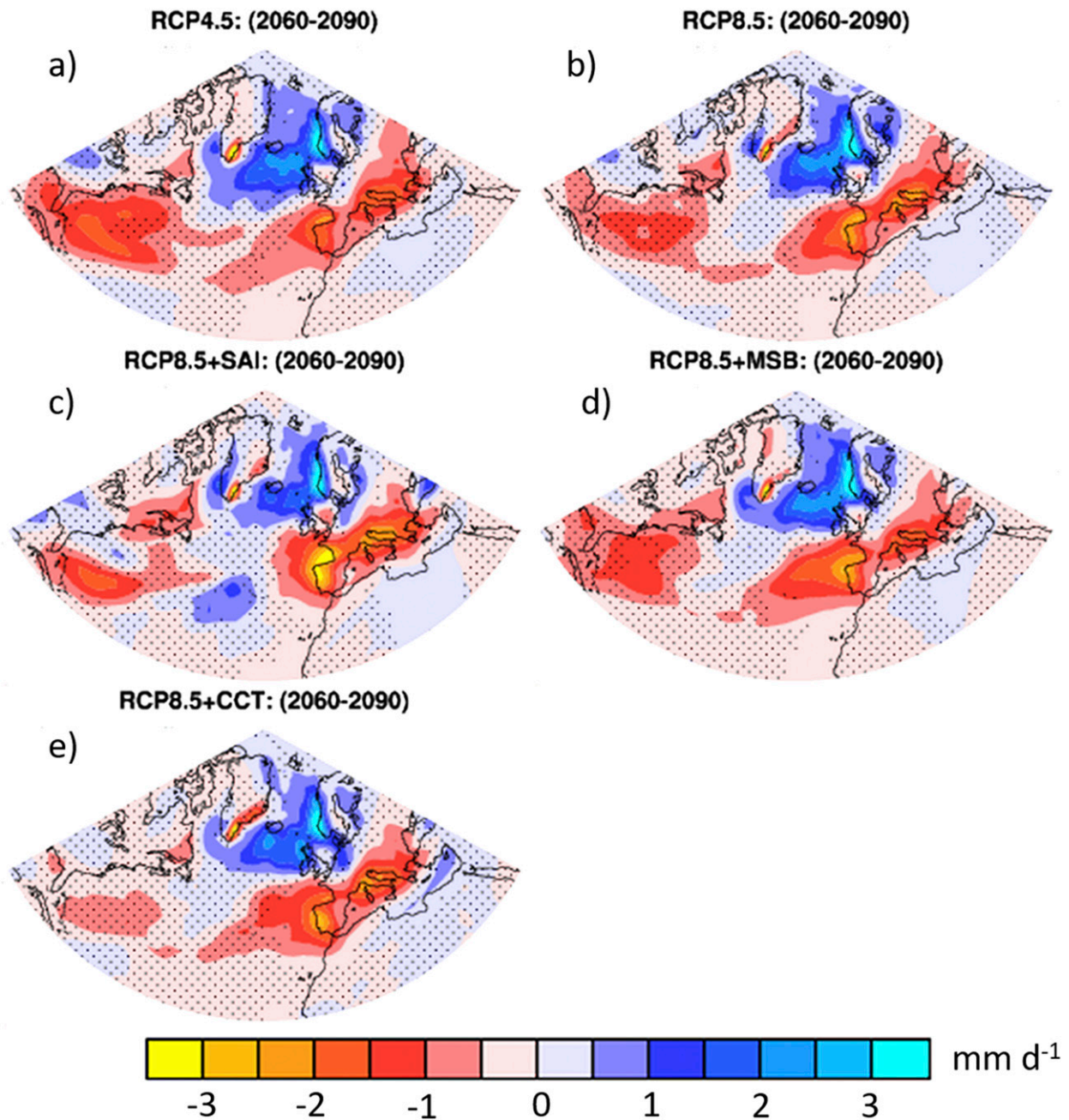


FIG. 8. DJFM precipitation rates (mm day^{-1}) for high minus low NAO composites. Only the indices greater than ± 1 standard deviation are considered for estimating the difference. Significant differences, at 95% confidence level following the Student's *t* test, are hatched.

heat capacity of the ocean compared to the other components in the climate system. Thus, the ocean heat content is a key metric in evaluating the response of the climate system to changes in radiative forcings. The simulated ocean heat content anomaly for the historical simulation follows the observations (Levitus et al. 2012) closely (reference period 1955–2005), with an increase of about $0.2 \times 10^{22} \text{ J yr}^{-1}$ over the late twentieth century

(Fig. 11a). The upper ocean heat content then rapidly increases in the RCP8.5 simulation, from $25 \times 10^{22} \text{ J}$ in 2020 to about $180 \times 10^{22} \text{ J}$ in year 2100 (Fig. 11a). In RCP4.5, the increase in heat content is limited to about $100 \times 10^{22} \text{ J}$ in 2100. The aerosol geoengineering cases remain fairly close to RCP4.5, although somewhat elevated toward the end of the century due to small net TOA fluxes throughout the century and thus a net gain

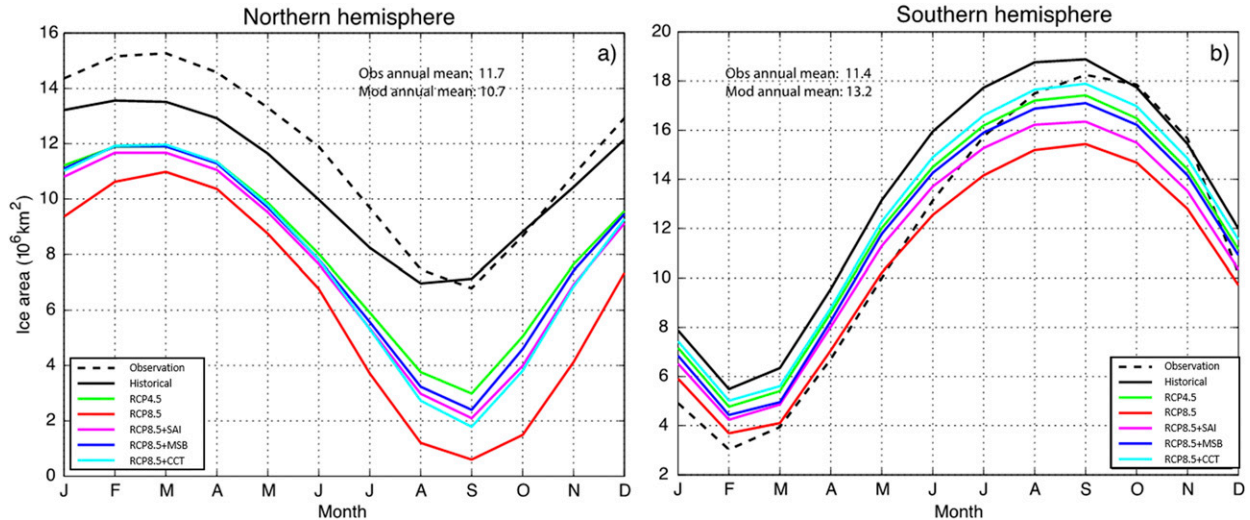


FIG. 9. (a) Arctic ($\times 10^6 \text{ km}^2$) and (b) Antarctic sea ice area ($\times 10^7 \text{ km}^2$). Monthly mean over years 2060–89. Red curves: RCP8.5, green: RCP4.5, purple: RCP8.5 + SAI, dark blue: RCP8.5 + MCB, light blue: RCP8.5 + CCT, solid black: historical simulation over years 1979–2005, and dashed black: observations from 1979–2005 (NSIDC; Cavalieri et al. 1996).

of energy. The top 700-m heat content in RCP8.5 + MSB and RCP8.5 + SAI is $\sim 10 \times 10^{22} \text{ J}$ higher than RCP4.5 at the end of the century. This is likely due to the buildup of heat before the climate engineering cases were branched off from RCP8.5 in year 2020, as discussed in section 3a, with also further investigation in section 3d. RCP8.5 + CCT increases the heat content a bit more during the last three decades, since the maximum radiative forcing was limited to -3.8 W m^{-2} . Hence, the higher radiative flux imbalance at the TOA in RCP8.5 + CCT at the end of the century contributes to the elevated heat content compared to the RCP4.5. Still, all three aerosol geoengineering methods reduce the increases in heat content relative to RCP8.5 substantially. After termination, there is a rapid increase of $\sim 3.6 \times 10^{22} \text{ J yr}^{-1}$, which is about twice the rate of increased ocean heat content in RCP4.5 toward the end of this century.

One of the most direct impacts of anthropogenic climate change is a rise in the global sea level (Church et al. 2013). Sea level rise is caused primarily by a combination of melting of ice sheets and glaciers and ocean thermal expansion. NorESM1-ME does not include melting of land ice, so in the following only the steric sea level changes are considered. The term *steric* here refers to the integral response to anomalies of the vertical density in the ocean, through temperature (thermsteric) and salinity (halosteric) variations. In terms of the global steric sea level changes, the RCP8.5 simulation suggests an increase of about 40 cm by the end of this century compared to early-twentieth-century levels (Fig. 11b). The RCP4.5 simulation results in a steric

sea level increase of about 30 cm. The SW-based climate geoengineering methods are found to almost completely push the steric sea level back to the RCP4.5 trajectory, while the RCP8.5 + CCT simulation resides slightly above the RCP4.5 level by the end of the century (Fig. 11b). Upon termination of the aerosol geoengineering in year 2101, a rapid acceleration of the steric sea level change is found reaching about 6 mm yr^{-1} .

The vertical structure of the steric sea level changes is illustrated in Fig. 12. Starting at the sea surface, the thermsteric and halosteric contributions from each level are cumulatively summed up over the ocean water column for different ocean subdomains for the period 2060–89. Generally, the thermsteric signal is much larger than any halosteric signal for all ocean basins. In the Atlantic, halosteric and thermsteric changes tend to somewhat compensate each other, although the thermsteric signals are typically 3 times as strong as the halosteric signals. Since the Atlantic is a region of active deepwater formation, most of the thermsteric changes occur within the upper 3000 m, while being fairly homogenous below that. In the Pacific and Indian Oceans, the thermsteric changes are typically confined to the upper 500–1000 m, and are also smaller than for the Atlantic. In the Southern Ocean both thermsteric and halosteric changes are evident throughout most of the water column, likely reflecting the intense vertical transfer of water properties in the Antarctic Circumpolar Current (e.g., Landerer et al. 2007). The aerosol geoengineering simulations are able to keep the vertical steric signals very close to the RCP4.5 levels. The

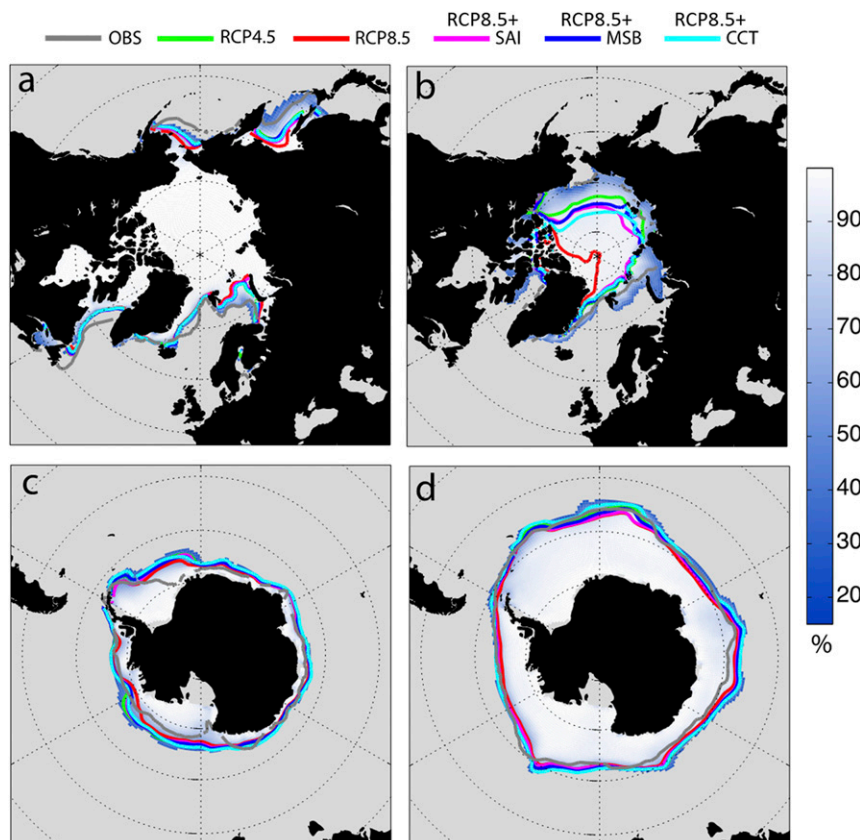


FIG. 10. Simulated and observed sea ice cover (defined at the 15% contour line) for (a) NH March, (b) NH September, (c) SH March, and (d) SH September. Blue shading shows the historical run monthly mean for 1955–2005. Gray curve shows the observed sea ice extent based on NCEP (1968–96). Monthly means over the period 2060–89. Red curves: RCP8.5, green: RCP4.5, purple: RCP8.5 + SAI, dark blue: RCP8.5 + MCB, light blue: RCP8.5 + CCT.

exception is the RCP8.5 + CCT simulation in the Atlantic, Pacific, and Indian Oceans, where the cumulative thermosteric signals are located about halfway between the RCP4.5 and RCP8.5 levels. This is from the regional differences in heat content change, which is governed by variations in air–sea heat fluxes and circulation changes. It has been found that ocean heat content increases more in the Atlantic over the past three decades (Palmer et al. 2017). Coincidentally, our simulations also show strongest and deepest thermosteric increase in the Atlantic.

The AMOC is projected to weaken substantially with global warming under the RCP8.5 scenario (Figs. 11c and 13b). By the end of this century, there is a decline of about 22% and 35% in the AMOC strength for the RCP4.5 and RCP8.5, respectively. These numbers are in line with estimates of future AMOC reduction based on CMIP5 models (Cheng et al. 2013). The weaker AMOC likely arises from a combination of reduced heat loss to the atmosphere and increasing freshwater fluxes at high

latitudes from precipitation and sea ice melting. Both of these factors have been shown to contribute to lighter surface waters and reduced deep convection in the northern sinking regions under twenty-first century greenhouse forcing (e.g., Thorpe et al. 2001). Compared with the RCP8.5 scenario all the geoengineering cases are found to restore the AMOC close to RCP4.5 levels, although a residual weakening (relative to RCP4.5) still remains (Figs. 13c,d). The mitigation of AMOC weakening in the geoengineering cases is qualitatively similar to what was found by Hong et al. (2017) when comparing the G1 scenario of GeoMIP with a $4\times\text{CO}_2$ scenario. The exact causes for the residual weakening found in our climate geoengineering cases are not clear, but could possibly be related to the way our experiments were set up. A more targeted aerosol injection at high latitudes could potentially give a more uniform cooling over the North Atlantic region, which could in turn contribute to a further strengthening of the AMOC compared to RCP8.5. A more detailed analysis of these aspects will,

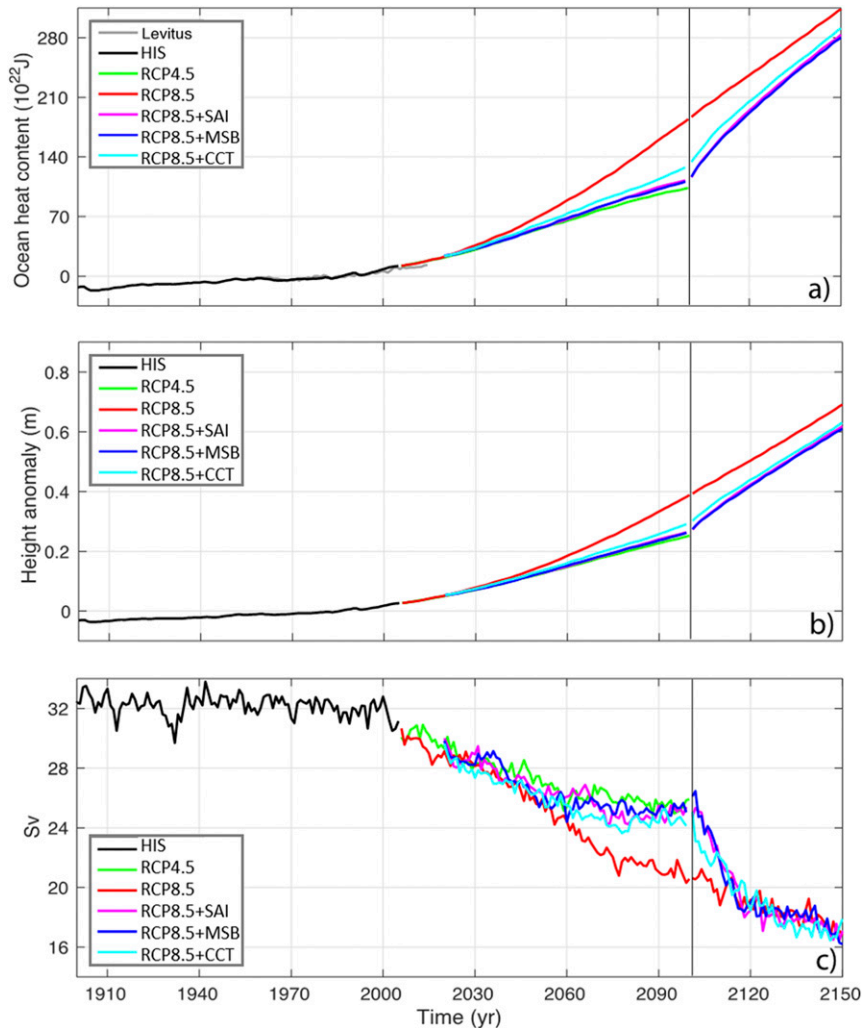


FIG. 11. Time series of the simulated ensemble mean (a) upper ocean heat content, (b) steric sea level, and (c) maximum Atlantic meridional overturning circulation strength. In (a) the observed upper ocean heat content based on Levitus et al. (2012) is shown in gray for comparison. Historical simulation (black), RCP4.5 (green), RCP8.5 (red), RCP8.5 + SAI (pink), RCP8.5 + MSB (blue), and RCP8.5 + CCT (cyan). The vertical line at year 2100 marks the termination of the climate geoengineering.

however, be reserved for future studies. After the sudden termination of the climate geoengineering in 2100, the AMOC strength decreases rapidly over a period of about 20 years, at which point it aligns closely with the RCP8.5 simulation (Fig. 11c).

In summary, our results suggest that the substantial weakening of the AMOC under the RCP8.5 scenario can clearly be mitigated using aerosol geoengineering. One of the many uncertainties regarding the future evolution of the AMOC is related to the potential melting of the Greenland ice sheet. To address this issue, a more realistic simulation in terms of Greenland ice sheet melting would be needed, either through additional sensitivity experiments (e.g., Swingedouw et al.

2015) or the inclusion of an interactive ice sheet model. This, however, is beyond the scope of this study.

d. Ocean and land carbon cycle

Since all experiments were performed with fully interactive carbon cycle, the atmospheric CO_2 concentrations are fully prognostic, taking into account changes in anthropogenic emissions as well as land and ocean fluxes. In all aerosol geoengineering experiments, CO_2 emissions follow the RCP8.5 scenario, and therefore the carbon cycle responses are mainly compared with the RCP8.5 baseline simulation. Considering this, the carbon cycle response in geoengineering experiments is expected to remain closer to this scenario than RCP4.5.

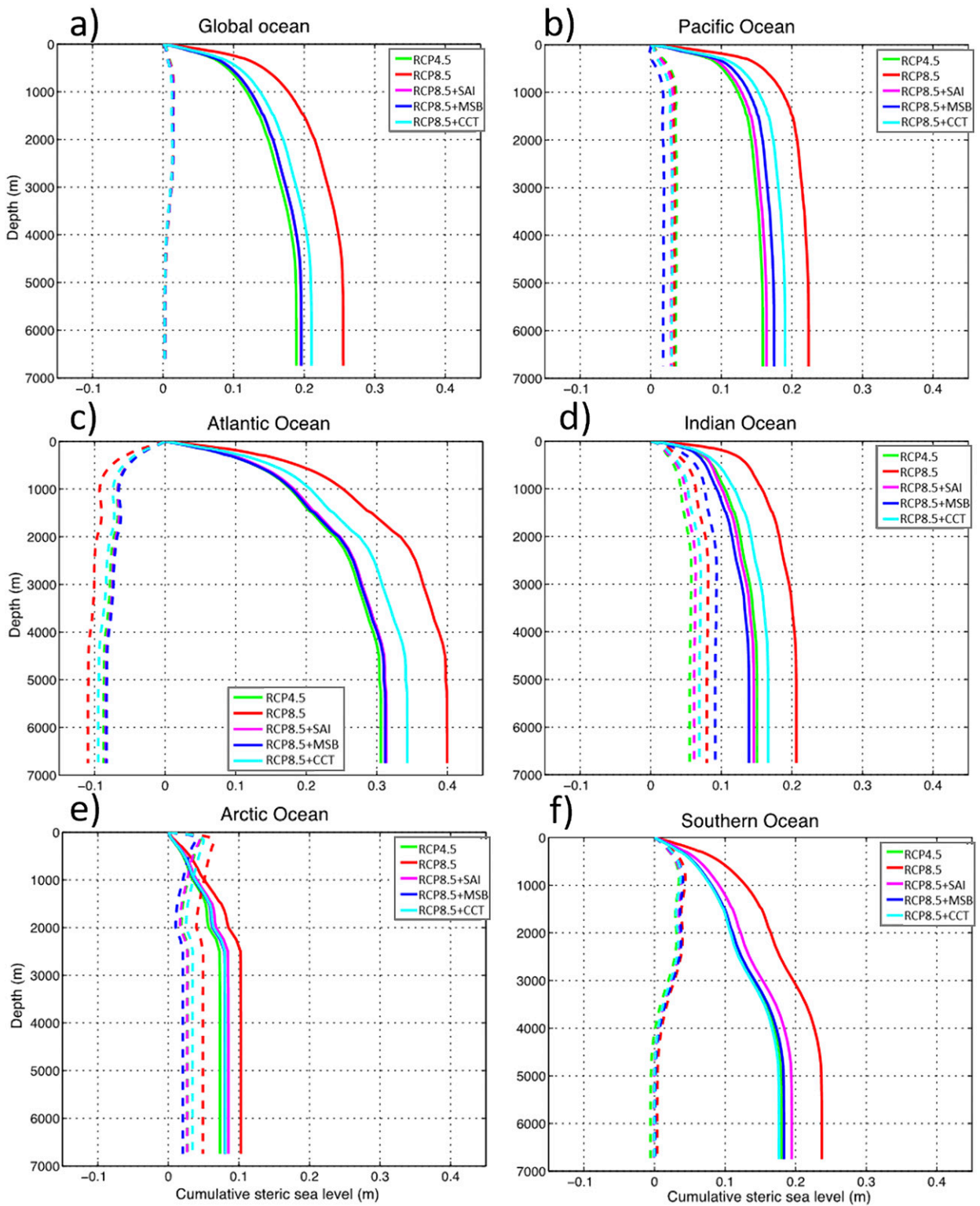


FIG. 12. Cumulative sum of thermosteric (solid lines) and halosteric (dashed lines) anomalies for different RCP scenarios across six ocean regions for the period 2060–89. Starting at the surface, the steric anomaly from each depth layer is added up. RCP4.5 (green), RCP8.5 (red), RCP8.5 + SAI (pink), RCP8.5 + MSB (blue), and RCP8.5 + CCT (cyan).

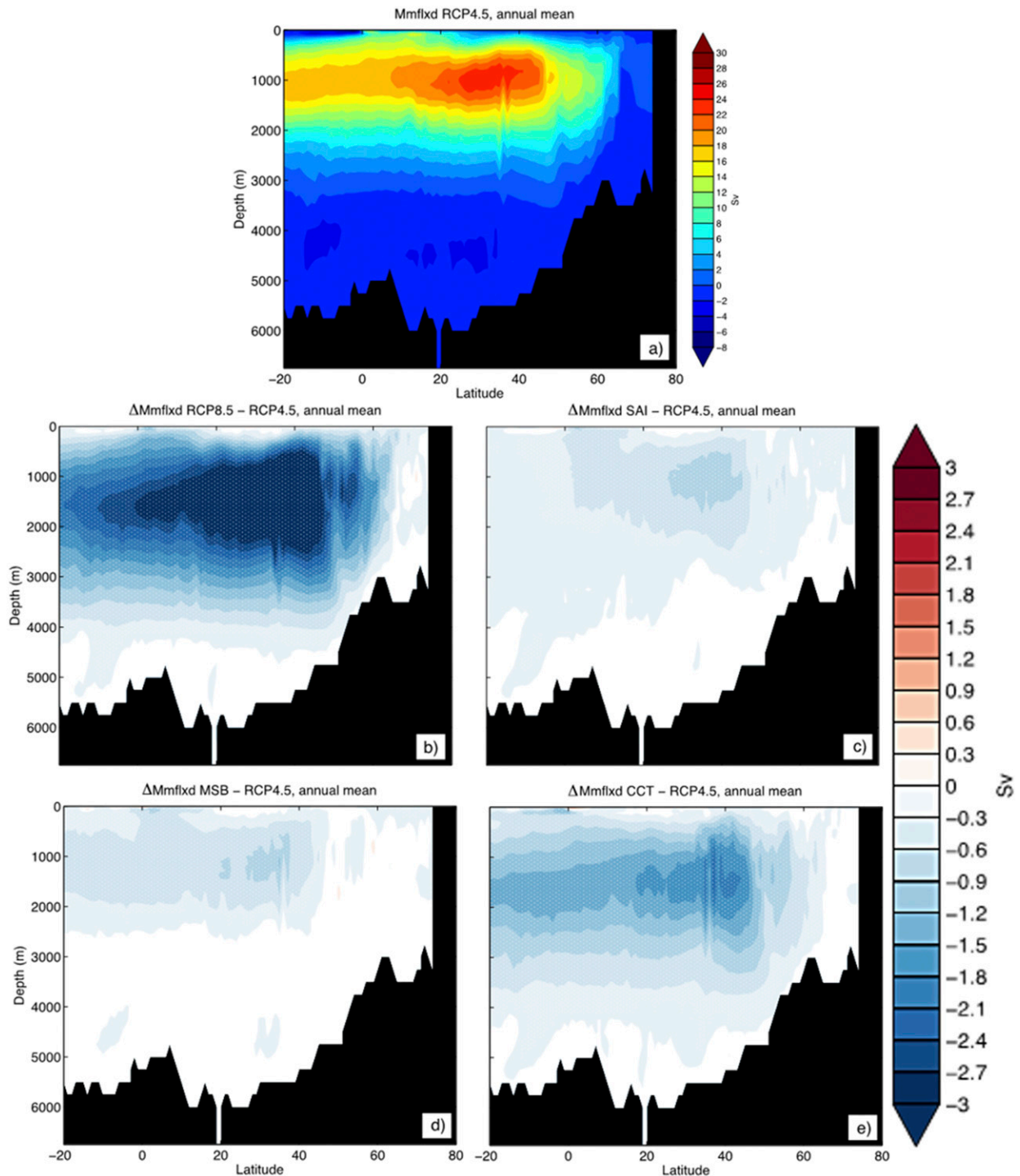


FIG. 13. (a) Annual mean Atlantic meridional streamfunction (Sv ; $1 \text{ Sv} \equiv 10^6 \text{ m}^3 \text{ s}^{-1}$) climatology for the years 2060–89 in RCP4.5. Differences from RCP4.5 in annual mean Atlantic meridional overturning circulation for (b) RCP8.5, (c) RCP8.5 + SAI, (d) RCP8.5 + MSB, and (e) RCP8.5 + CCT.

The emission-driven NorESM1-ME RCP4.5 simulation projects an atmospheric CO_2 concentration of 588 ppm at the end of this century. This is higher than in the concentration-driven scenario, which has 570 ppm.

The emission-driven RCP8.5 scenario also ends up with a higher atmospheric CO_2 concentration than the concentration-driven one due to carbon cycle feedbacks, with 1097 ppm in year 2100 compared to 936 ppm.

TABLE 3. Cumulative global land and ocean carbon uptakes (in Pg C units).

Experiment	Ocean		Land	
	2020–2100	2101–50	2020–2100	2101–50
RCP45	263.61	—	201.84	—
RCP85	449.33	290.64	282.23	289.57
RCP8.5 + SAI	464.97	287.76	288.19	299.47
RCP8.5 + MSB	464.70	288.64	295.70	290.68
RCP8.5 + CCT	467.52	287.69	300.22	292.77

Considering that the experiments were designed to offset the anthropogenic radiative forcing difference between the concentration-driven RCP8.5 and RCP4.5, the larger difference in radiative forcing between the corresponding emissions-driven scenarios were not taken into account when deriving the amount of aerosol geoengineering to apply. The CO₂ radiative forcing difference between the emission-driven RCP8.5 and RCP4.5 and the concentration-driven counterparts amounts to a difference of 1.6 W m⁻², assuming a radiative forcing efficiency for CO₂ of 0.0143 W m⁻² ppm⁻¹ (Forster et al. 2007). This contributes to the additional warming in the aerosol geoengineering cases compared to RCP4.5.

Under the RCP8.5 simulation, the global mean atmospheric CO₂ is projected to increase by 665 ppm by the end of the twenty-first century relative to year 2020. Because of increases in ocean and land carbon sinks of 15–18 and 6–18 Pg C respectively (Table 3), the projected atmospheric CO₂ increases are marginally reduced by aerosol geoengineering and results in atmospheric CO₂ concentrations of 1095, 1087, and 1092 ppm with RCP8.5 + SAI, RCP8.5 + MSB, and RCP8.5 + CCT respectively in 2100 (Fig. 14). The reductions in the atmospheric CO₂ concentrations by the aerosol geoengineering corresponds to a reduction of -0.17 to -0.28 W m⁻² from reducing the concentrations by -12 to -20 ppm, or -25 to -42 Pg C. Our results show that the carbon cycle reduction on the atmospheric concentrations are minimal compared to mitigation requirements of RCP4.5. As Keith et al. (2017) largely get their estimates of carbon-climate feedback from collections of models that do not have terrestrial nitrogen limitation, they are likely to be overestimating the land carbon uptake.

Aerosol geoengineering induced increases in the ocean carbon sink compared to RCP8.5 becomes apparent toward the end of the twenty-first century (Fig. 14c), specifically in the North Atlantic. Under the RCP8.5, a reduced AMOC strength, as discussed in section 3b, leads to a reduction in anthropogenic carbon uptake in the North Atlantic. In all three aerosol injection experiments, this AMOC reduction is alleviated (Fig. 13), and

consequently the carbon sink is stronger compared to RCP8.5 (see also Tjiputra et al. 2016). While the evolutions of the globally integrated ocean carbon sinks are similar in the different aerosol geoengineering cases (Fig. 14c), the response in the net primary production is more variable. In our RCP8.5 + CCT simulation, the projected global ocean net primary production (NPP) maintain values close to the contemporary period, and even higher than the RCP4.5 scenario at the end of the twenty-first century. Both RCP8.5 + SAI and RCP8.5 + MSB still produce a pronounced negative trend in NPP, although smaller than the RCP8.5 simulation. Changes in the ocean NPP are largely associated with changes in the large-scale ocean circulation, and a more detailed and regional impact analysis of these different aerosol forcings on the regional ocean carbon cycle is provided in Lauvset et al. (2017).

Similar to the ocean, all aerosol geoengineering cases increase the land carbon sinks, as shown in Table 3. The effects of changes to the ratio of direct to diffuse light on photosynthesis is included in the model, which has been shown to be an important aspect of aerosol geoengineering (Xia et al. 2016). Of the three methods, RCP8.5 + CCT simulates the largest land carbon increase over the full 2020–2100 period. Changes in the land carbon sink predominantly translate to higher vegetation and soil carbon pools. The overall impacts of the different land managements between RCP4.5 and RCP8.5 are smaller than the soil carbon pool response to the aerosol geoengineering (Fig. 14e). There is a steady increase in the soil carbon pools in all the aerosol geoengineering experiments peaking at ~15 Pg C yr⁻¹, with RCP8.5 + MSB yielding a somewhat smaller increase by end of the twenty-first century with regard to RCP8.5 (Figs. 14d,e). Except for a few regions, the changes in the vegetation carbon pool are much more variable and could largely be attributed to the regionally varying precipitation response simulated in the different experiments (Fig. S7). This is consistent with earlier findings by Tjiputra et al. (2016), who show that the regional vegetation carbon change in the NorESM1-ME is sensitive to change in the precipitation patterns (Fig. S2).

Upon termination of aerosol geoengineering, the rates of ocean and land carbon uptakes revert to the background RCP8.5 scenario (Figs. 14b,c). This signal is most pronounced in the ocean, where the accumulated carbon uptake from 2101 to 2150 only differs by ~1% from RCP8.5 (Table 3). Over land, the vegetation carbon content increases over the next 50 years following termination, while soil carbon decreases in all three different aerosol geoengineering simulations. Even though the soil carbon decreases, it remains higher than the RCP8.5 simulation. This implies that a large portion

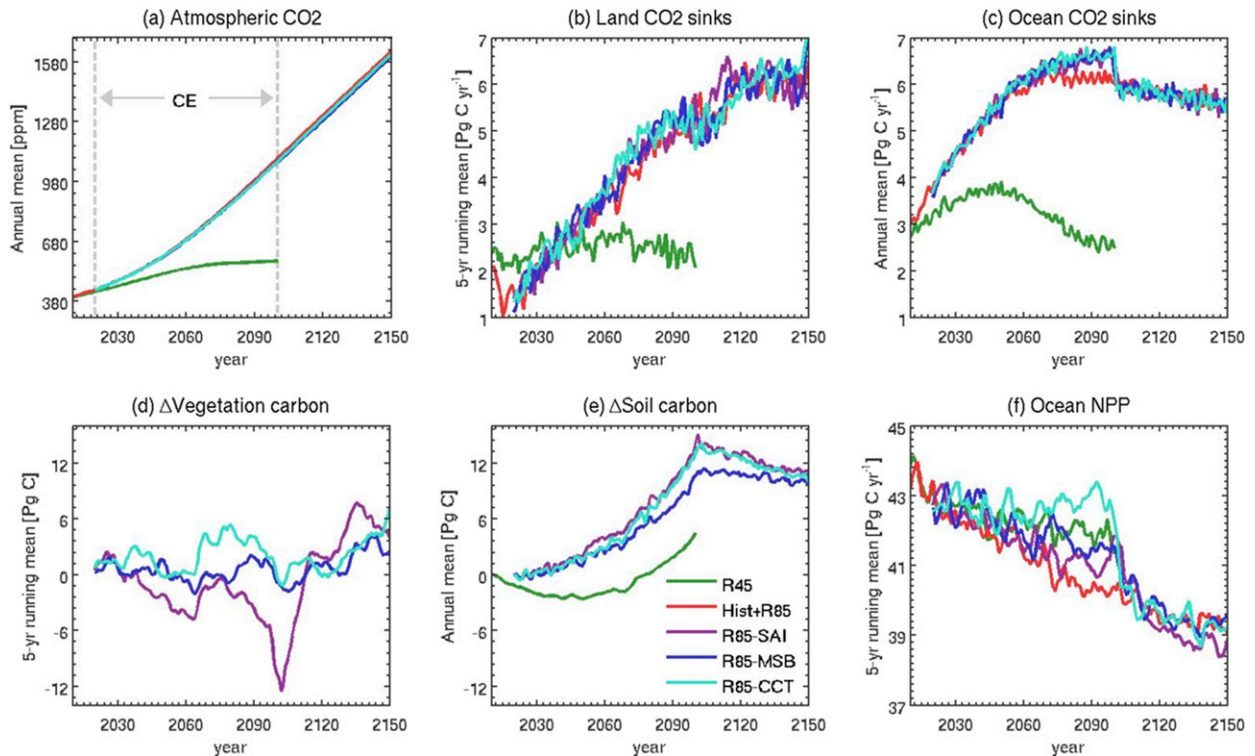


FIG. 14. Time series of projected global mean (a) atmospheric CO_2 concentration [ppm], (b) land CO_2 sinks [Pg C yr^{-1}], (c) ocean CO_2 sinks [Pg C yr^{-1}], (d) changes in vegetation carbon pools [Pg C], (e) changes in soil carbon pools [Pg C], and (f) ocean net primary production [Pg C yr^{-1}]. Vertical dashed lines in (a) show the period of aerosol injection implementation. Values in (a) and (c) are annual mean whereas those in (b), (d), (e), and (f) are 5-yr running mean; (d) and (e) show changes relative to RCP8.5.

of the land carbon sink increase attributed by aerosol geoengineering is retained for at least 50 years following the cessation.

4. Summary and conclusions

This work assesses the climate response to three different aerosol geoengineering techniques in depth in a scenario where the anthropogenic radiative forcing in the RCP8.5 scenario is brought down to that of RCP4.5 through these methods individually. The climate geoengineering techniques considered here are stratospheric aerosol injections, marine sky brightening, and cirrus cloud thinning. We found that a radiative forcing difference of $+4.0 \text{ W m}^{-2}$, corresponding to the difference between the concentration-driven RCP8.5 and RCP4.5 in year 2100, could be offset by the three approaches considered, except for the case of RCP8.5 + CCT. The maximum effective radiative forcing achievable from RCP8.5 + CCT was found to be of -3.8 W m^{-2} in our model, NorESM1-ME, yielding a somewhat higher radiative flux imbalance at the TOA than RCP8.5 + SAI, RCP8.5 + MSB, and RCP4.5 toward the end of this century. We conclude that all three aerosol-based techniques

would potentially exert a large enough radiative forcing to contribute toward reaching ambitious climate targets, such as those set by the Paris Agreement.

The climate states of the aerosol geoengineering cases are mostly closer to the RCP4.5 climate than RCP8.5 and many anthropogenic global warming symptoms are alleviated. There are, however, notable differences in the resulting climate due to the nature of the forcings applied and lack of mitigation, as summarized below.

CCT acts mainly on the LW part of the radiation budget, as opposed to MSB and SAI, yielding a difference in the response, particularly for the hydrological cycle. RCP8.5 + MSB and RCP8.5 + SAI see a weakening of the hydrological cycle from the reduction in latent heat flux from the surface due to less incoming solar radiation at the surface. RCP8.5 + MSB also experiences stronger precipitation over tropical land, due to the “monsoon-like” response to the inhomogeneous forcing pattern. RCP8.5 + CCT, on the other hand, results in an enhancement of the hydrological cycle. The reduction in the lifetime and thickness of the LW trapping ice clouds results in an increase in the latent heat flux from the surface as the atmosphere is attempting to restore its energetic equilibrium.

Our idealized climate geoengineering simulations show less sea ice losses than RCP4.5. However, some residual polar heat is still found, especially in the Arctic, in the aerosol geoengineering cases, resulting in a somewhat reduced sea ice cover compared to RCP4.5. In the SH, one side effect includes a pronounced overcooling of surface air temperature in the RCP8.5 + CCT case and a sea ice cover increase compared to the RCP4.5 case. The ocean heat content, steric sea level, and Atlantic meridional overturning circulation are all seen to be almost fully ameliorated to RCP4.5 levels when using the stratospheric sulfate injections or marine sky brightening as climate geoengineering approaches. The cirrus cloud thinning method is able to alleviate some of the projected ocean heat and circulation changes in RCP8.5 (~69%), but not all. Furthermore, the rebound to the RCP8.5 ocean state after the climate geoengineering is abruptly terminated produces a very large rate of thermosteric sea level rise—about 6 mm yr^{-1} —which is more than twice the current sea level rise. Melting of land-based ice sheets and glaciers would potentially further accelerate this rate, but is not accounted for in the model. The AMOC shows an abrupt reduction of more than 30% in the first 15 years after termination of the aerosol geoengineering. This illustrates just how vulnerable the climate would be to any unforeseen disruptions to climate geoengineering (e.g., Baum et al. 2013; Jones et al. 2013).

The patterns of regional atmospheric variability over the North Atlantic, represented by the NAO, appear to be most sensitive to the SAI forcing among the three techniques. The anomalous equatorial heating produced in the lower stratosphere by the injection of aerosols tends to strengthen the NAO circulation.

Unlike its efficiency in offsetting the anthropogenic radiative forcing, aerosol geoengineering does little to offset the CO_2 concentrations in the atmosphere. All three approaches only marginally enhance carbon removal from the atmosphere. These aerosol injection geoengineering approaches cannot be seen as substitutes for emission reductions as the result is a rather different looking climate. Questions remain whether these types of climate action would reduce some aspects of global harm, and work toward helping the sustainable development goals, compared to global warming. No clear “showstoppers” were identified for any of the approaches in this study (i.e., there is no evidence of negative impacts worse than the unabated global warming of RCP8.5). Showstoppers could still arise in the technical realization of such technologies, however, or in physical processes that are not explicitly simulated in the model. The aerosol geoengineering methods would be nonrestorative of the climate to an unperturbed state, and new and different

climate conditions would result from any such large-scale deployment. Neither would all symptoms of climate change be addressed by such forms of geoengineering. The atmospheric CO_2 burden with associated feedbacks on the carbon cycle, including ocean acidification for instance, would not be alleviated.

It is worth keeping in mind that aerosol implemented in the model is represented in a simplified way, and there are a number of uncertainties and unknowns related in particular to aerosol–cloud–climate interactions. This is a multimethod single model study, and results would need to be confirmed by other models, or real-world experiments, to fully assess robustness.

This work does not advocate the real-world deployment of aerosol geoengineering. It attempts only to explore the possible climate responses and differences in response between such methods.

Acknowledgments. RCN project EXPECT, Grant 229760/E10. H.M. was also funded by RCN Grant 261862/E10. The simulations were performed on resources provided by UNINETT Sigma2—the National Infrastructure for High Performance Computing and Data Storage in Norway, accounts nn9182k, nn9448k, NS2345K, and NS9033K. Data are available upon request.

REFERENCES

- Ahlm, L., A. Jones, C. W. Stjern, H. Muri, B. Kravitz, and J. E. Kristjánsson, 2017: Marine cloud brightening—As effective without clouds. *Atmos. Chem. Phys.*, **17**, 13 071–13 087, <https://doi.org/10.5194/acp-17-13071-2017>.
- Albrecht, B. A., 1989: Aerosols, cloud microphysics, and fractional cloudiness. *Science*, **245**, 1227–1230, <https://doi.org/10.1126/science.245.4923.1227>.
- Alterskjær, K., and J. E. Kristjánsson, 2013: The sign of the radiative forcing from marine cloud brightening depends on both particle size and injection amount. *Geophys. Res. Lett.*, **40**, 210–215, <https://doi.org/10.1029/2012GL054286>.
- , —, O. Boucher, H. Muri, U. Niemeier, H. Schmidt, M. Schulz, and C. Timmreck, 2013: Sea-salt injections into the low-latitude marine boundary layer: The transient response in three Earth system models. *J. Geophys. Res. Atmos.*, **118**, 12 195–12 206, <https://doi.org/10.1002/2013JD020432>.
- Andrews, T., and P. M. Forster, 2010: The transient response of global-mean precipitation to increasing carbon dioxide levels. *Environ. Res. Lett.*, **5**, 025212, <https://doi.org/10.1088/1748-9326/5/2/025212>.
- , —, and J. M. Gregory, 2009: A surface energy perspective on climate change. *J. Climate*, **22**, 2557–2570, <https://doi.org/10.1175/2008JCLI2759.1>.
- Aswathy, V. N., O. Boucher, M. Quaas, U. Niemeier, H. Muri, J. Mülmenstädt, and J. Quaas, 2015: Climate extremes in multi-model simulations of stratospheric aerosol and marine cloud brightening climate engineering. *Atmos. Chem. Phys.*, **15**, 9593–9610, <https://doi.org/10.5194/acp-15-9593-2015>.
- Bala, G., K. Caldeira, R. Nemani, L. Cao, G. Ban-Weiss, and H. J. Shin, 2011: Albedo enhancement of marine clouds to counteract global

- warming: Impacts on the hydrological cycle. *Climate Dyn.*, **37**, 915–931, <https://doi.org/10.1007/s00382-010-0868-1>.
- Baum, S. D., T. M. Maher Jr., and J. Haqq-Misra, 2013: Double catastrophe: Intermittent stratospheric geoengineering induced by societal collapse. *Environ. Syst. Decis.*, **33**, 168–180, <https://doi.org/10.1007/s10669-012-9429-y>.
- Benduhn, F., J. Schallock, and M. G. Lawrence, 2016: Early growth dynamical implications for the steerability of stratospheric solar radiation management via sulfur aerosol particles. *Geophys. Res. Lett.*, **43**, 9956–9963, <https://doi.org/10.1002/2016GL070701>.
- Boucher, O., and Coauthors, 2013: Clouds and aerosols. *Climate Change 2013: The Physical Science Basis*, T. F. Stocker et al., Eds., Cambridge University Press, 571–658.
- Broccoli, A. J., K. A. Dahl, and R. J. Stouffer, 2006: Response of the ITCZ to Northern Hemisphere cooling. *Geophys. Res. Lett.*, **33**, L01702, <https://doi.org/10.1029/2005GL024546>.
- Budyko, M. I., 1977: On present-day climatic changes. *Tellus*, **29**, 193–204, <https://doi.org/10.3402/tellusa.v29i3.11347>.
- Cavalieri, D. J., C. L. Parkinson, P. Gloersen, and H. J. Zwally, 1996: Sea ice concentrations from Nimbus-7 SMMR and DMSP SSM/I-SSMIS passive microwave data, version 1 (updated yearly). NASA National Snow and Ice Data Center Distributed Active Archive Center, accessed 3 December 2016, <https://doi.org/10.5067/8GQ8LZQVLOVL>.
- Cheng, W., J. C. H. Chiang, and D. Zhang, 2013: Atlantic meridional overturning circulation (AMOC) in CMIP5 models: RCP and historical simulations. *J. Climate*, **26**, 7187–7197, <https://doi.org/10.1175/JCLI-D-12-00496.1>.
- Chiang, J. C. H., and C. M. Bitz, 2005: Influence of high latitude ice cover on the marine intertropical convergence zone. *Climate Dyn.*, **25**, 477–496, <https://doi.org/10.1007/s00382-005-0040-5>.
- Church, J. A., and Coauthors, 2013: Sea level change. *Climate Change 2013: The Physical Science Basis*, T. F. Stocker et al., Eds., Cambridge University Press, 1137–1216.
- Clarke, L., and Coauthors, 2014: Assessing transformation pathways. *Climate Change 2014: Mitigation of Climate Change*, O. Edenhofer et al., Eds., Cambridge University Press, 413–510.
- Collins, M., and Coauthors, 2013: Long-term climate change: Projections, commitments and irreversibility. *Climate Change 2013: The Physical Science Basis*, T. F. Stocker et al., Eds., Cambridge University Press, 1029–1136.
- Crook, J. A., L. S. Jackson, S. M. Osprey, and P. M. Forster, 2015: A comparison of temperature and precipitation responses to different Earth radiation management geoengineering schemes. *J. Geophys. Res. Atmos.*, **120**, 9352–9373, <https://doi.org/10.1002/2015JD023269>.
- Crutcher, P. J., 2006: Albedo enhancement by stratospheric sulfur injections: A contribution to resolve a policy dilemma? *Climatic Change*, **77**, 211–219, <https://doi.org/10.1007/s10584-006-9101-y>.
- Driscoll, S., A. Bozzo, L. J. Gray, A. Robock, and G. Stenchikov, 2012: Coupled Model Intercomparison Project 5 (CMIP5) simulations of climate following volcanic eruptions. *J. Geophys. Res.*, **117**, D17105, <https://doi.org/10.1029/2012JD017607>.
- Forster, P., and Coauthors, 2007: Changes in atmospheric constituents and in radiative forcing. *Climate Change 2007: The Physical Science Basis*, S. Solomon et al., Eds., Cambridge University Press, 129–234.
- Gasparini, B., S. Münch, L. Poncet, M. Feldmann, and U. Lohmann, 2017: Is increasing ice crystal sedimentation velocity in geoengineering simulations a good proxy for cirrus cloud seeding? *Atmos. Chem. Phys.*, **17**, 4871–4885, <https://doi.org/10.5194/acp-17-4871-2017>.
- Hanna, E., T. E. Cropper, P. D. Jones, A. A. Scaife, and R. Allan, 2014: Recent seasonal asymmetric changes in the NAO (a marked summer decline and increased winter variability) and associated changes in the AO and Greenland blocking index. *Int. J. Climatol.*, **35**, 2540–2554, <https://doi.org/10.1002/joc.4157>.
- Hong, Y., J. C. Moore, S. Jevrejeva, D. Ji, S. J. Phipps, A. Lenton, S. Tilmes, S. Watanabe, and L. Zhao, 2017: Impact of the GeoMIP G1 sunshade geoengineering experiment on the Atlantic meridional overturning circulation. *Environ. Res. Lett.*, **12**, 034009, <https://doi.org/10.1088/1748-9326/aa5fb8>.
- Hurrell, J. W., Y. Kushnir, G. Ottersen, and M. Visbeck, 2003: An overview of the North Atlantic Oscillation. *The North Atlantic Oscillation: Climatic Significance and Environmental Impact*, *Geophys. Monogr.*, Vol. 134, Amer. Geophys. Union, 1–35, <https://doi.org/10.1029/134GM01>.
- Jones, A., J. Haywood, and O. Boucher, 2011: A comparison of the climate impacts of geoengineering by stratospheric SO₂ injection and by brightening of marine stratocumulus cloud. *Atmos. Sci. Lett.*, **12**, 176–183, <https://doi.org/10.1002/asl.291>.
- , and Coauthors, 2013: The impact of abrupt suspension of solar radiation management (termination effect) in experiment G2 of the Geoengineering Model Intercomparison Project (GeoMIP). *J. Geophys. Res. Atmos.*, **118**, 9743–9752, <https://doi.org/10.1002/jgrd.50762>.
- Keith, D. W., G. Wagner, and C. L. Zabel, 2017: Solar geoengineering reduces atmospheric carbon burden. *Nat. Climate Change*, **7**, 617–619, <https://doi.org/10.1038/nclimate3376>.
- Kellogg, W. W., and S. H. Schneider, 1974: Climate stabilization: For better or for worse? *Science*, **186**, 1163–1172, <https://doi.org/10.1126/science.186.4170.1163>.
- Kravitz, B., and Coauthors, 2013: An energetic perspective on hydrological cycle changes in the Geoengineering Model Intercomparison Project. *J. Geophys. Res. Atmos.*, **118**, 13 087–13 102, <https://doi.org/10.1002/2013JD020502>.
- , and Coauthors, 2015: The Geoengineering Model Intercomparison Project phase 6 (GeoMIP6): Simulation design and preliminary results. *Geosci. Model Dev.*, **8**, 3379–3392, <https://doi.org/10.5194/gmd-8-3379-2015>.
- , D. G. MacMartin, M. J. Mills, J. H. Richter, S. Tilmes, J.-F. Lamarque, J. J. Tribbia, and F. Vitt, 2017: First simulations of designing stratospheric sulfate aerosol geoengineering to meet multiple simultaneous climate objectives. *J. Geophys. Res. Atmos.*, **122**, 12 616–12 634, <https://doi.org/10.1002/2017JD026874>.
- Kristjánsson, J. E., H. Muri, and H. Schmidt, 2015: The hydrological cycle response to cirrus cloud thinning. *Geophys. Res. Lett.*, **42**, 10 807–10 815, <https://doi.org/10.1002/2015GL066795>.
- Landerer, F. W., J. H. Jungclauss, and J. Marotzke, 2007: Regional dynamic and steric sea level change response to the IPCC-A1B scenario. *J. Phys. Oceanogr.*, **37**, 296–312, <https://doi.org/10.1175/JPO3013.1>.
- Latham, J., 1990: Control of global warming? *Nature*, **347**, 339–340, <https://doi.org/10.1038/347339b0>.
- Lauvset, S. K., J. Tjiputra, and H. Muri, 2017: Climate engineering and the ocean: Effects on biogeochemistry and primary production. *Biogeosciences*, **14**, 5675–5691, <https://doi.org/10.5194/bg-14-5675-2017>.
- Lee, J., P. Yang, A. E. Dessler, B.-C. Gao, and S. Platnik, 2009: Distribution and radiative forcing of tropical thin cirrus clouds. *J. Atmos. Sci.*, **66**, 3721–3731, <https://doi.org/10.1175/2009JAS3183.1>.
- Levitus, S., and Coauthors, 2012: World Ocean heat content and thermocline sea level change (0–2000 m), 1955–2010. *Geophys. Res. Lett.*, **39**, L10603, <https://doi.org/10.1029/2012GL051106>.

- Li, J.-L. F., and Coauthors, 2012: An observationally based evaluation of cloud ice water in CMIP3 and CMIP5 GCMs and contemporary reanalyses using contemporary satellite data. *J. Geophys. Res.*, **117**, D16105, <https://doi.org/10.1029/2012JD017640>.
- McClellan, J., D. W. Keith, and J. Apt, 2012: Cost analysis of stratospheric albedo modification delivery systems. *Environ. Res. Lett.*, **7**, 034019, <https://doi.org/10.1088/1748-9326/7/3/034019>.
- Meinshausen, M., and Coauthors, 2011: The RCP greenhouse gas concentrations and their extensions from 1765 to 2300. *Climatic Change*, **109**, 213–241, <https://doi.org/10.1007/s10584-011-0156-z>.
- Mitchell, D. L., 1996: Use of mass- and area-dimensional power laws for determining precipitation particle terminal velocities. *J. Atmos. Sci.*, **53**, 1710–1723, [https://doi.org/10.1175/1520-0469\(1996\)053<1710:UOMAAD>2.0.CO;2](https://doi.org/10.1175/1520-0469(1996)053<1710:UOMAAD>2.0.CO;2).
- , and W. Finnegan, 2009: Modification of cirrus clouds to reduce global warming. *Environ. Res. Lett.*, **4**, 045102, <https://doi.org/10.1088/1748-9326/4/4/045102>.
- Muri, H., J. E. Kristjánsson, T. Storelvmo, and M. A. Pfeffer, 2014: The climatic effects of modifying cirrus clouds in a climate engineering framework. *J. Geophys. Res. Atmos.*, **119**, 4174–4191, <https://doi.org/10.1002/2013JD021063>.
- , U. Niemeier, and J. E. Kristjánsson, 2015: Tropical rainforest response to marine sky brightening climate engineering. *Geophys. Res. Lett.*, **42**, 2951–2960, <https://doi.org/10.1002/2015GL063363>.
- National Research Council, 2015: *Climate Intervention: Reflecting Sunlight to Cool Earth*. The National Academies Press, 260 pp., <https://doi.org/10.17226/18988>.
- Niemeier, U., and C. Timmreck, 2015: What is the limit of climate engineering by stratospheric injection of SO₂? *Atmos. Chem. Phys.*, **15**, 9129–9141, <https://doi.org/10.5194/acp-15-9129-2015>.
- , H. Schmidt, and C. Timmreck, 2011: The dependency of geoengineered sulfate aerosol on the emission strategy. *Atmos. Sci. Lett.*, **12**, 189–194, <https://doi.org/10.1002/asl.304>.
- , —, K. Alterskjær, and J. E. Kristjánsson, 2013: Solar irradiance reduction via climate engineering: Impact of different techniques on the energy balance and the hydrological cycle. *J. Geophys. Res. Atmos.*, **118**, 11 905–11 917, <https://doi.org/10.1002/2013JD020445>.
- Oleson, K. W., G. B. Anderson, B. Jones, S. A. McGinnis, and B. Sanderson, 2018: Avoided climate impacts of urban and rural heat and cold waves over the U.S. using large climate model ensembles for RCP8.5 and RCP4.5. *Climatic Change*, **146**, 377–392, <https://doi.org/10.1007/s10584-015-1504-1>.
- O'Neill, B. C., and Coauthors, 2018: The benefits of reduced anthropogenic climate change (BRACE): A synthesis. *Climatic Change*, **146**, 287–301, <https://doi.org/10.1007/s10584-017-2009-x>.
- Palmer, M. D., and Coauthors, 2017: Ocean heat content variability and change in an ensemble of ocean reanalyses. *Climate Dyn.*, **49**, 909–930, <https://doi.org/10.1007/s00382-015-2801-0>.
- Robock, A., D. G. MacMartin, R. Duren, and M. W. Christensen, 2013: Studying geoengineering with natural and anthropogenic analogs. *Climatic Change*, **121**, 445–458, <https://doi.org/10.1007/s10584-013-0777-5>.
- Salter, S., G. Sortino, and J. Latham, 2008: Sea-going hardware for the cloud albedo method of reversing global warming. *Philos. Trans. Roy. Soc. London*, **366A**, 3989–4006, <https://doi.org/10.1098/rsta.2008.0136>.
- Schäfer, S., and Coauthors, 2015: The European transdisciplinary assessment of climate engineering (EuTRACE): Removing greenhouse gases from the atmosphere and reflecting sunlight away from Earth. European Union Seventh Framework Programme Coordination and Support Action Rep., 169 pp.
- Schmidt, H., and Coauthors., 2012: Solar irradiance reduction to counteract radiative forcing from a quadrupling of CO₂: Climate responses simulated by four Earth system models. *Earth Syst. Dyn.*, **3**, 63–78, <https://doi.org/10.5194/esd-3-63-2012>.
- Shepherd, J., and Coauthors, 2009: Geoengineering the climate: Science, governance and uncertainty. Royal Society Rep., 83 pp.
- Stenchikov, G., A. Robock, V. Ramaswamy, M. D. Schwarzkopf, K. Hamilton, and S. Ramachandran, 2002: Arctic Oscillation response to the 1991 Mount Pinatubo eruption: Effects of volcanic aerosols and ozone depletion. *J. Geophys. Res.*, **107**, 4803, <https://doi.org/10.1029/2002JD002090>.
- Stjern, C. W., and Coauthors, 2018: Response to marine cloud brightening in a multi-model ensemble. *Atmos. Chem. Phys.*, **18**, 621–634, <https://doi.org/10.5194/acp-18-621-2018>.
- Storelvmo, T., J. E. Kristjánsson, H. Muri, M. Pfeffer, D. Barahona, and A. Nenes, 2013: Cirrus cloud seeding has potential to cool climate. *Geophys. Res. Lett.*, **40**, 178–182, <https://doi.org/10.1029/2012GL054201>.
- Swingedouw, D., C. B. Rodehacke, S. M. Olsen, M. Menary, Y. Gao, U. Mikolajewicz, and J. Mignot, 2015: On the reduced sensitivity of the Atlantic overturning to Greenland ice sheet melting in projections: A multi-model assessment. *Climate Dyn.*, **44**, 3261–3279, <https://doi.org/10.1007/s00382-014-2270-x>.
- Tebaldi, C., and M. F. Wehner, 2018: Benefits of mitigation for future heat extremes under RCP4.5 compared to RCP8.5. *Climatic Change*, **146**, 349–361, <https://doi.org/10.1007/s10584-016-1605-5>.
- Thorpe, R. B., J. M. Gregory, T. C. Johns, R. A. Wood, and J. F. B. Mitchell, 2001: Mechanisms determining the Atlantic thermohaline circulation response to greenhouse gas forcing in a non-flux-adjusted coupled climate model. *J. Climate*, **14**, 3102–3116, [https://doi.org/10.1175/1520-0442\(2001\)014<3102:MDTATC>2.0.CO;2](https://doi.org/10.1175/1520-0442(2001)014<3102:MDTATC>2.0.CO;2).
- Tilmes, S., and Coauthors, 2015: A new Geoengineering Model Intercomparison Project (GeoMIP) experiment designed for climate and chemistry models. *Geosci. Model Dev.*, **8**, 43–49, <https://doi.org/10.5194/gmd-8-43-2015>.
- Tjiputra, J. F., C. Roelandt, M. Bentsen, D. M. Lawrence, T. Lorentzen, J. Schwinger, Ø. Seland, and C. Heinze, 2013: Evaluation of the carbon cycle components in the Norwegian Earth System Model (NorESM). *Geosci. Model Dev.*, **6**, 301–325, <https://doi.org/10.5194/gmd-6-301-2013>.
- , A. Grini, and H. Lee, 2016: Impact of idealized future stratospheric aerosol injection on the large-scale ocean and land carbon cycles. *J. Geophys. Res. Biogeosci.*, **121**, 2–27, <https://doi.org/10.1002/2015JG003045>.
- Twomey, S., 1977: The influence of pollution on the shortwave albedo of clouds. *J. Atmos. Sci.*, **34**, 1149–1152, [https://doi.org/10.1175/1520-0469\(1977\)034<1149:TIOPOT>2.0.CO;2](https://doi.org/10.1175/1520-0469(1977)034<1149:TIOPOT>2.0.CO;2).
- UNFCCC, 2015: Adoption of the Paris Agreement. United Nations Framework Convention on Climate Change Rep., 32 pp.
- Vellinga, M., and R. A. Wood, 2002: Global climatic impacts of a collapse of the Atlantic thermohaline circulation. *Climatic Change*, **54**, 251–267, <https://doi.org/10.1023/A:1016168827653>.
- Weisenstein, D. K., D. W. Keith, and J. A. Dykema, 2015: Solar geoengineering using solid aerosol in the stratosphere. *Atmos. Chem. Phys.*, **15**, 11 835–11 859, <https://doi.org/10.5194/acp-15-11835-2015>.
- Xia, L., A. Robock, S. Tilmes, and R. R. Neely III, 2016: Stratospheric sulfate geoengineering could enhance the terrestrial photosynthesis rate. *Atmos. Chem. Phys.*, **16**, 1479–1489, <https://doi.org/10.5194/acp-16-1479-2016>.